Journal of Architectural Environment & Structural Engineering Research

Journal of Architectural Environment &Structural Engineering Research

Editor-in-Chief

Dr. Kaveh Ostad-Ali-Askari

Contents

REVIEW

Knot Types Used by Transformable and Rigid Linear Structural Systems

Mª Dolores Álvarez Elipe[*]

Estética y Teoría de las Artes, URJC, Madrid, Spain

ABSTRACT

A knot is the joining place between two or more constructive elements in a framework or structure. They have a fundamental importance in the structure, according to their design they will be able to give a geometric configuration or another to the system and will also absorb certain forces or others. Depending on the movements they allow to the bars, there are rigid knots, articulated knots and slip knots. In this paper a study of cases about rigid knots or embedments used by structural systems so far will be presented. These types of knots prevent the rotation and movement of the constructive elements used for construction. In this paper also a study of cases about the articulated and slip knots used by transformable structural systems so far will be presented. An articulated knot allows the rotation but not the movement of the elements. A slip knot prevents movement in one of the three axes of the reference system, but not in the others, nor in the rotation between the elements. The research is focused on presenting a summary and comparison of rigid knots, articulated knots and slip knots that have been used in the structural design of some architecture. The union systems research will be crucial in this study. The investigation shows an important state of the art that provides technical solutions to apply on novel architectures based on rigid structural systems and articulated and slip structural systems. The research is useful to produce the current constructive solutions based on these constructive systems.

1. Introduction

According to construpedia [1]:

A rigid knot is the type of knot that avoids turns and displacements of the elements. It is called embedment too.

An articulated knot is the type of knot that allows the rotation but not the movement of the elements. It is called articulation too.

A slip knot is the type of knot that prevents movement in one of the three axes of the reference system, but not in the others, nor in the rotation between the elements.

The research is focused in summarize and compare types of rigid knots, articulated knots and slip knots that have been used in the structural design of some architecture. The research of adequate forms and geometries will be crucial in this study. The investigation presents an important state of the art that provides technical solutions to apply on novel architectures based on rigid, articulated and slip

Corresponding Author:
Mª Dolores Álvarez Elipe,
Estética y Teoría de las Artes, URJC, Madrid, Spain;
Email: mdolores_500@hotmail.com

structural systems. The research is useful to produce the current constructive solutions based on these constructive systems.

The goal is to understand any current rigid, articulated and slip knots to know their configuration and the advantages and disadvantages of them. It is collected for the knowledge of rigid, articulated and slips knots to the artists, architects, engineers and all types of people.

Some examples of this rigid knots are Pyramitec, Tridimatec, Unibat, Sphérobat, Trio-detic, Segmo, Tubaccord, Bourquardez, Begue, Chamayou, Begue-kieffer, Delacrix-glotin-monier-sejournet, Kieffer, Sarton, Spherical, Bitubular, Tesep, Unistrut, Mero, Wupperman…

Examples of some type of articulated and slip knots will be presented too. These types of knots are inside of this classification: knots by rotation of the bar, hinged knots, bolted or pin knots and knots per bearing. Authors like Fuller, Pérez Piñero, Albert Moore, Zeigler, Swetish and Baumann, Daniel S-H Lee, Olga Popovic Larsen and Seung-Deog Kim, SeungDeog KIM, SunKyeong PARK, JePil JANG, InA SIN, JangBog LEE, ChangWoo HA and SeungTeak JUNG, Yohei Yokosuka and Teruo Matsuzawa, Jesús Anaya, Mª Dolores Álvarez and Ramón Serrano will be studied.

The research is supported by geometrical basic criteria.

2. Knot Types Used by Rigid Linear Structural Systems

The evolution of rigid knots will be studied to generate a synthesis of the novelties than have been developed in this area. All of that is possible because of the study of some authors and some existing patents.

2.1 Stéphane du Château

Stéphane du Château [2] is a French-Polish architect and urban planner that invents the construction systems as Pyramitec, Tridimatec, Unibat and Sphérobat knots.

Du Château created his first system of spatial structure – the tri-directional SDC (Figure 1) in 1956 [3]. He obtained his patent in 1957 and after he applied it to cover the lobby of the power station on the Grandval Dam (1957-1958), designed by the architect H. Marty [4,5]. The knot can be used to single layer tights. They are prepared to the assembly and welding of the concurrent bars. The knots have been used in double layer tights, attaching the diagonal bars to the shells. The tube bars are welded to the nodes after the adjustment of the whole structure.

The SDC knot resolved three problems mainly [2]:

Every knot receives six members.
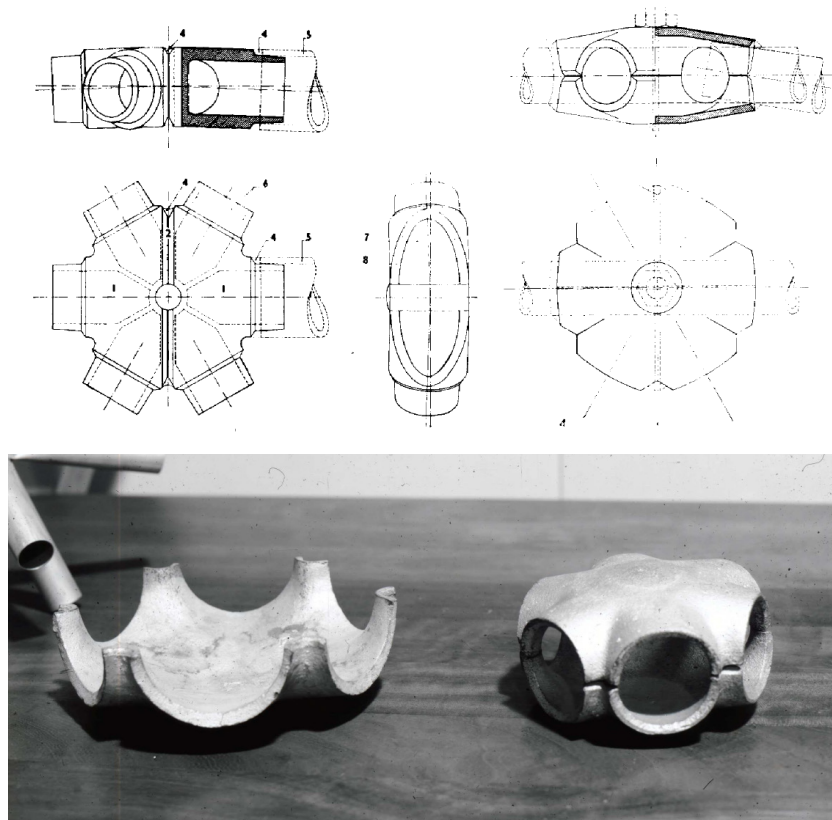
The constraint length is resolved independently of the

Figure 1. SDC knot, draws and prototype, Stéphane du Château (1956) [2]

tube length introduced into the node. All members can have the same size. The variations are absorbed by the penetration length into the node.

The curvature is possible. The spaces into the knot allow proportionate the required limb inclination (only a few degrees are enough).

Later, he discovered a new system which led him to develop four construction patents, many realizations and publications in the 1960s. Realizing the difficulty of in situ welding in construction, Stéphane du Château proposed the Pyramitec system (Figure 2), where the connections are realized by the use of screws [4]. This system is characterized by the application of pyramids that determine the inertia of the structure. It was used in the realization of the National Exposition Fair of Nancy (1963-1964, by the architects M. Kruger and M. Pierron).

It is formed by a cylindrical central body that can receive the bars of one level of the mesh. It also has a truncated cone, where the diagonal bars are screwed. To make this system prefabricated is feasible. The assembly is easy and it is preferably done on the ground and standing up after assembly. These structures used as roofs, can adopt flat, inclined, slightly curved shapes and in certain cases they can form domes.

The pyramids could not exceed three meters due to the transportation. By this reason Stéphane du Château proposed the Tridimatec System (Figures 3 and 4). It is constituted by the use of beams in meshes, where their ends are connected in such a way that they form a system of crossed beams [5]. With an accessory formed by two crossed plates, the possible number of concurrent bars in this node is increased.
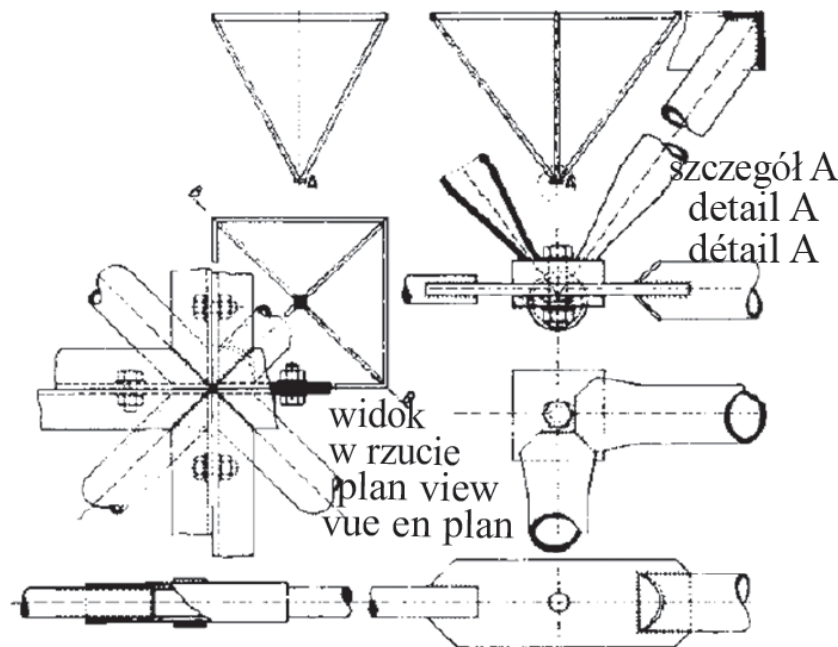

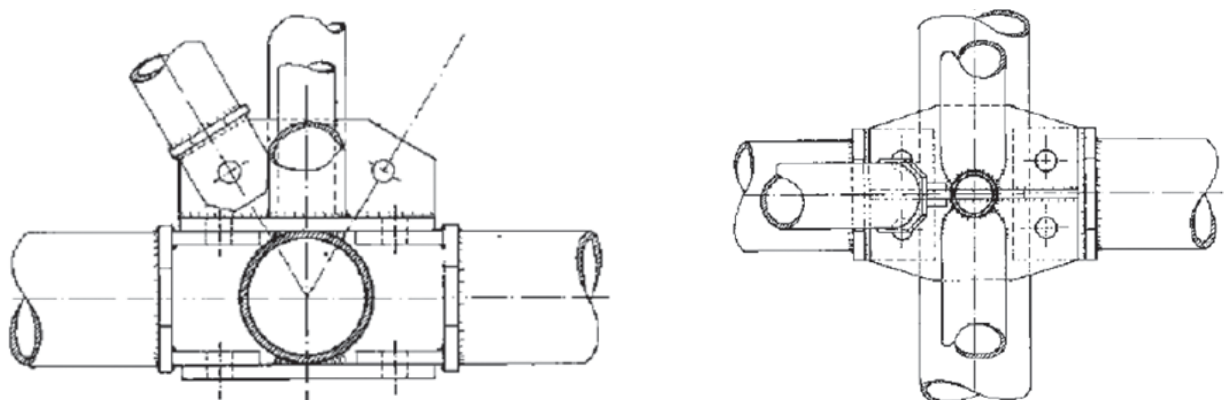**Figure 2.** Ortogonal System Pyramitec (pyramid with square base), Stéphane du Château (1963) [4]

Figure 3. Draws of details of Tridimatec system: view of the connector for a two-dimensional grid, Stéphane du Château (1964) [5]
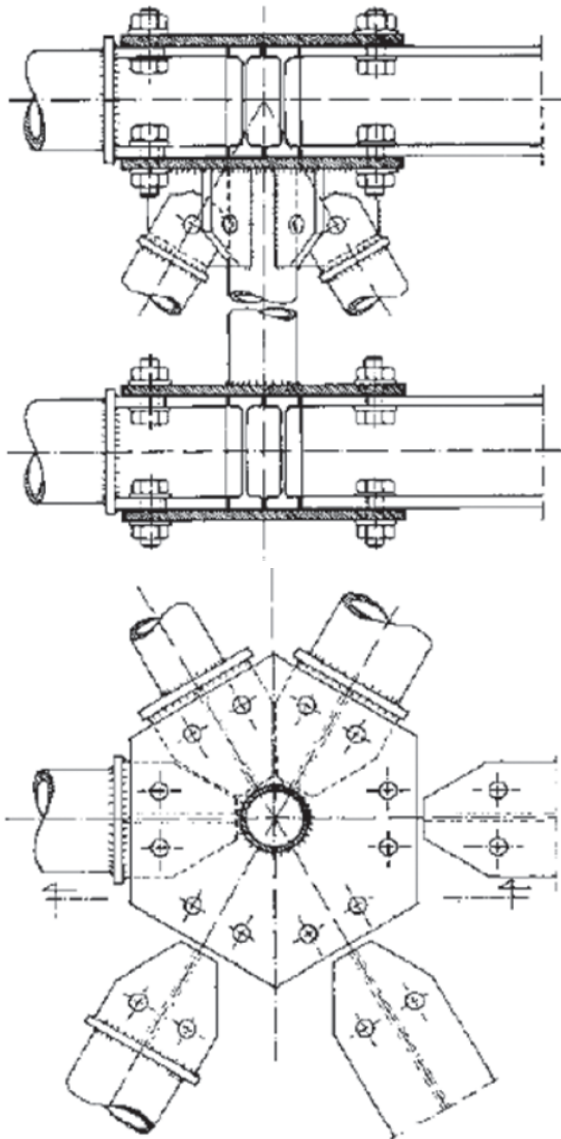
Figure 4. Draws of details of Tridimatec system: view of the connector for a three-dimensional grid, Stéphane du Château (1964) [5]

The great flexibility of the Pyramitec system application, with its different geometries of construction elements, evolves towards the Unibat system (Figure 5). The geometry of Unibat is formed by a board of pyramids and squares [5]. It only covers the 50% of the surfaces with pyramids, which is more economic. The square-based pyramids are connected in pairs using one of their base angles and connecting their tops with bars. This connection corresponds to a three-dimensional structure with two parallel layers. The meshes of the superior layer are constituted by the bases of the pyramid and they are oriented 45º in relation with the layers of the inferior layer, constituted by bars that merge the ends of the pyramids. This system is useful, according to its scale, to

make slabs, roofs or urban macrostructures. This system has good behavior in an immense variety of programs and, mainly during the 1970s; its efficiency was proved by carrying out fifty projects in France and abroad.

Figure 5. Unibat system, Stéphane Du Château (1970) [5]

Even though Unibat was successful, Du Château's realizations needed another system with nodes and members, which were easier to transport than the pyramids. All specialists knew about the success of the "Mero" knot in these years, and took advantage of the competition for the Baltimore airport (1975) to use it. However, Du Château designs a perforated sphere that can receive the members. Afterwards, the investigation of a spherical knot which set of members could have any relative position, end up developing the Spherobat knot (Figure 6). This knot is realized with two pieces: one of these is the third part of a sphere; the other is two thirds of the sphere [5].
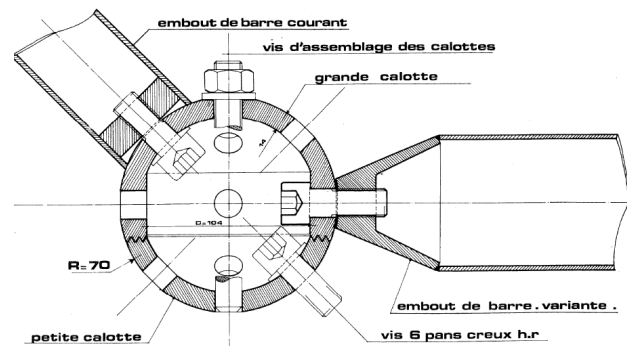
Figure 6. Spherobat, Stéphane Du Château (1975) [5]

Apart of the knots realized by Stéphane Du Château, it is realized a classification of rigid knots, presented in continuation.

2.2 Trio-detic Knot

The Trio-detic system (Figure 7) is originally from Canada. This system was developed during 1950's by the Fentiman Bros Company [6]. The patent is to be used in a reticulate of three directions. The bars are plane in their ends and they are introduced by pressure in serrated grooves that exist in the knots. The principal characteristic is that the union of the bars is realized with no welding, no bolts and no rivets. The distribution of the bars that go to the node determines its shape.

Figure 7. Trio-detic knot, Fentiman Bros Company [6]

The knot of the Trio-detic system will be the base of the design of some prefabricated systems, like the protected ones under the patent WO 2006097545 A1, whose date of presentation is 16th March 2005 and its date of publication is 21st September 2006. Its inventor is Juan Carracedo Planelles and the solicitant is Montur Estan, S.L. [7].

2.3 Makowski Dome Knot

The knots of Makowski dome (Figure 8) are metal caps to which the tubular bars are attached by means of pins [8].
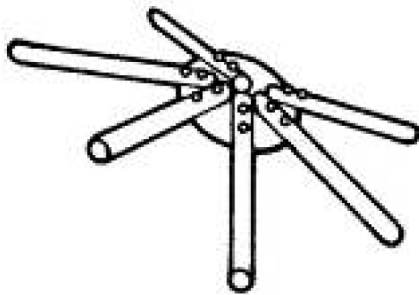
Figure 8. Makowski dome knot [8]

2.4 Segmo Knot

Segmo Knots (Figure 9) are welded steel. It is composed by two parts: one spherical and one prismatic. The bars are fixed by welding or by any other mechanical means [8].

It is a variant of the previous one; the tubes have at their ends a stem that is inserted into existing holes in the node. It allows joining by rivets and bolts with the annular disk of both parts.
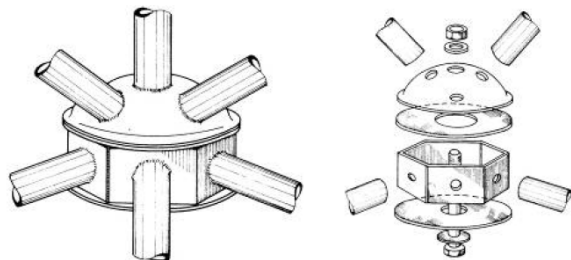
Figure 9. Segmo knot [8]

2.5 Tubaccord Knot

In the Tubaccord knot (Figure 10) the tubular bars are either directly welded or fixed by means of pins that fit into grooves located at the ends of the bars and in a sleeve previously welded to the bar of greater diameter concurrent to the node [8].
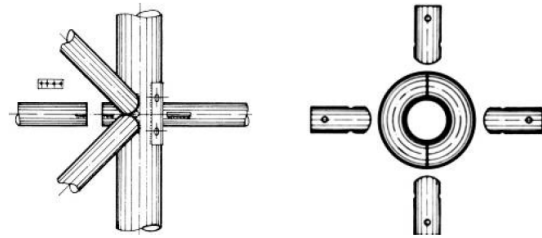
Figure 10. Tubaccord knot [8]

2.6 Bourquardez Knot

The bourquardez knot (Figure 11) is composed by one or some torus, obtained by joining two 180º elbows and tubular sleeves welded to said torus. The concurrent bars in the node are attached to the sleeves by means of riveting [8].

Figure 11 represented a knot prepared to meshes of one layer and one knot to meshes of two layers.
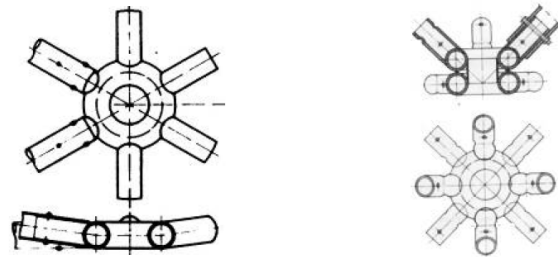
Figure 11. Bourquardez knot [8]

2.7 Begue Knot

The Begue knot (Figure 12) is formed by a nucleus to which the bars with frustoconical ends are screwed [8].
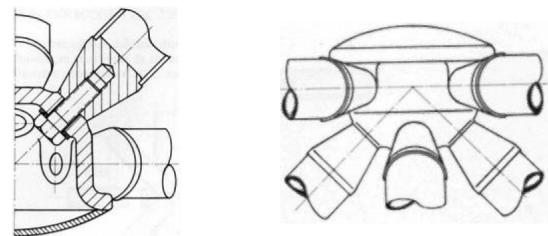
Figure 12. Begue knot [8]

2.8 Chamayou Knot

The Chamayou knots (Figure 13) can be planes, flanged along a closed polygonal line, or cubic or tetrahedral in shape, with the same flanges on each of the edges. The flanges are squares, polygonal sections or with the shape of a surface of revolution (cylinder, torus, etc.), and to

them the tubular bars are fixed by means of clamps [8].

Figure 13 represented a plane knot with hexagonal shape.
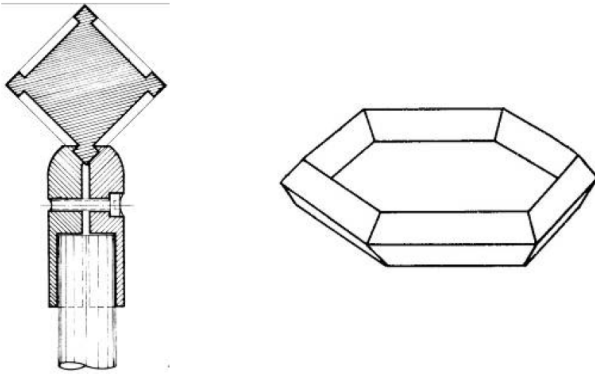
Figure 13. Chamayou knot [8]

2.9 Begue-kieffer Knot

The Begue-kieffer knot (Figure 14) is formed by a sphere with some starts with two grooves in order to fix the tubes [8].

This fixing is carried out by means of a hydraulic group, located on the ground, which presses a collar arranged around the tube and on the grooves of the boot, previously inserted on it. This is how the bar fits into the boot through the slots.
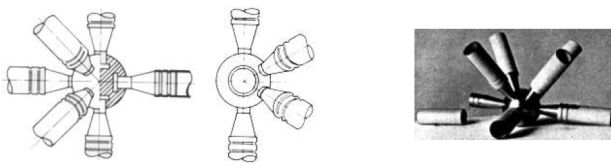
Figure 14. Begue-kieffer knot [8]

2.10 Delacrix-glotin-monier-sejournet Knot

Delacrix-glotin-monier-sejournet knot (Figure 15) is formed by one or two semi-tubes with welded fins that indicate the directions of the concurrent bars. These semi-tubes are joined by means of rivets or welding to the concurrent bar of greater diameter of the node. The remaining bars are fixed by crushing their ends and joining them, by means of welding or pins, to the fins [8].
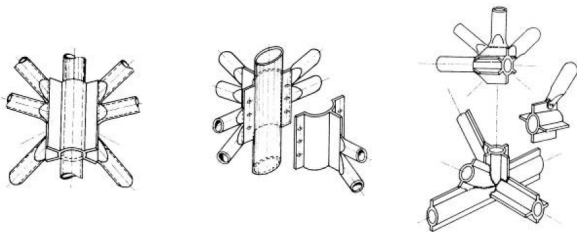
Figure 15. Delacrix-glotin-monier – sejournet knot [8]

2.11 Kieffer Knot

Kieffer knot (Figure 16) is formed by a solid central cylinder, its function is to be the pin for the entire knot, which consists of two concentric cylinders, the outer one with grooves that hold the welded ribs at the ends of the concurrent bars [8].
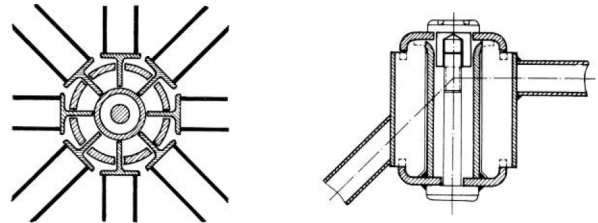
Figure 16. Kieffer knot [8]

2.12 Sarton Knot

The process to obtain the Sarton knot (Figure 17) consists in flattening the pipes at the points corresponding to a knot, in order to be able to cross them comfortably and place a pin with a fixing thread [8].
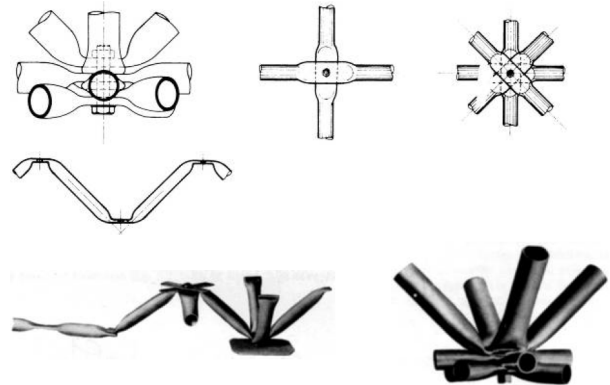

Figure 17. Sarton knot [8]

2.13 Spherical Knot

The Spherical knot (Figure 18) is constituted by a sphere where bars are joined, by welding, in any direction. To absorb differences in the tube lengths, a sleeve with a greater diameter is welded to the node. The sphere is usually filled with mortar as safety against possible sagging of itself [8].
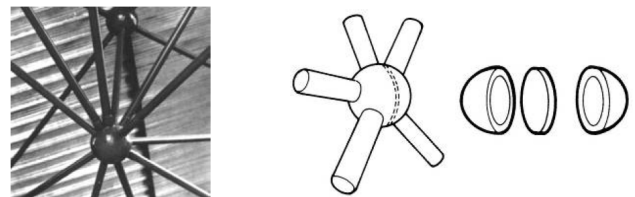
Figure 18. Spherical knot [8]

2.14 Bi-tubular Knot

The Bi-tubular knot (Figure 19) is constituted by two tubes, joined in parallel, where the concurrent bars are welded [8].
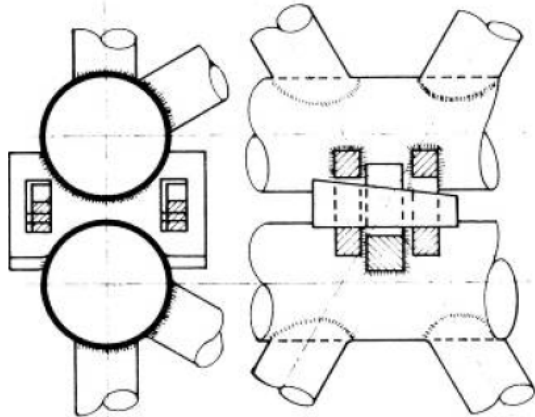
Figure 19. Bi-tubular knot [8]

2.15 Tesep Knot

The concurrent bars in the Tesep knot (Figure 20) are joined directly by welding to the larger diameter or by screwing ribs, welded at their ends, to a plate that is also welded and perpendicular to the central tube [8].
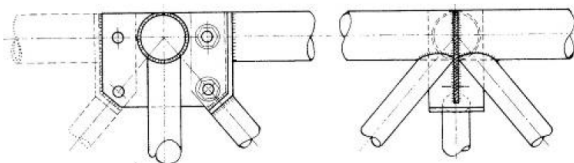
Figure 20. Tesep knot [8]

2.16 Unistrut Knot

The Unistrut knot [5] consist in the utilization of two pieces of folded sheet metal that overlap and where the bars are attached by pins (Figure 21). The bars are profiled and the knots mare made of stamped sheet metal. In this system, all the elements used have the same length and are joined by identical devices.
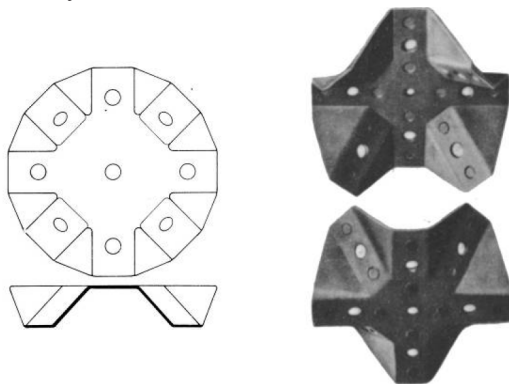
Figure 21. Unistrut knot [5]

2.17 Mero knot

The Mero structural system [4] is employed in tubular constructions of steel to fixed and provisional type works (fixed warehouses, frame structures, scaffolding, supports, etc.). It is formed by octagons, inscribed in a sphere, where a previously prepared bar can be screwed.

The MERO system was used by Mengeringhausen before of the Second World War.

Its two basic elements are: the connection spheres in which 18 octagons are inscribed with one threaded hole for each one and the bars that are threaded into the holes. The bars length must be equal.

Every knot can group the ends of the 18 bars without eccentricity. It is a light system that permits a maximum of prefabrication and in the assembly, specialized personnel is not necessary. The usual meshes are:

Squares of 0.5 m; 1.0 m; 2.0 m side and their corresponding diagonals.

Those formed by equilateral triangles of 0.7 m; 1.4 m or 2.8 m on a side.

This results in angles of 45°, 60° or 90° respectively, between the bars.

The Mero structures can be assembled quickly with unskilled labor. The transport of the elements is easy and cheap. The system is very flexible in terms of the variety of geometric shapes that it can adopt.
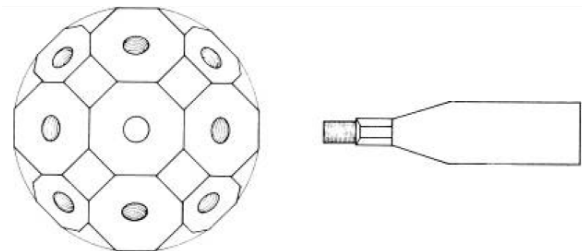
Figure 22. Mero knot [4]

2.18 Wupperman knot

The Wupperman knot (Figure 23) developed by the sign of Theodor Wupperman is used in spatial reticular systems of one layer. It is formed by a hexagon where the concurrent bars are screwed in six possible directions. The bars are profiled [8].
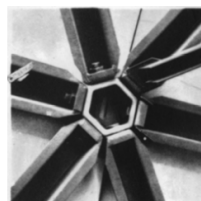
Figure 23. Wupperman knot [8]

3. Knot Type Used by Transformable Structural Systems

The evolution of articulated and slip knots will be studied to generate a synthesis of the novelties than have been developed in this area. All of this is possible because of the study of some authors and some existing patents.

3.1 Knots Classification of Transformable Structural Systems According to Their Movements

All transformable structure needs mechanisms in the joints to realize the process of pliability, unfolding, opening, closed or deformed. First of all, it is possible to determine that the movements in the joins can be in the plane or in the space. The movements of one bar in the plane are three: one turn and two displacements "u" and "v". But in the space, one bar has six possible movements: 3 turns and 3 displacements.

When the book "Synthesis of mechanisms" of Nieto [9] is revised, it can be said that the kinematic torque is the joint, with the faculty of movement, of two bars, so that the bars present a relative movement of certain characteristics due to the constraints imposed by this joint. According to the geometric locus described by any point of a bar in the relative movement of both, they are classified into: first degree or linear pairs, if the locus is a line; second degree or surface pairs, if the locus is a surface; and third degree or spatial pairs, if the locus is a region of space (Figure 24).

According to the degrees of freedom number possessed by the relative movement of the two bars that make up the pair, they are classified into: pairs of one, two, three, four and five degrees of freedom, or pairs of class I, II, III, IV and V, respectively (Figure 25).

Rodríguez [10] attempts to summarize the types of nodes regardless of the conditions of the members (Figure 26).

The first two, rotating and hinged knots, are simple solutions that can be located in the center of the bar or at its ends. The last two cases, pin knot and rolling, are more complex. In addition to rotating the bar, the entire structure changes its position. In these types of knot, the clearances are an important requirement to allow the passage of the bar through its different stages.

3.2 Patents of Knots of Transformable Structural Systems

In continuation, the knots that have been emerging as patents since deployable bar structures began to be developed and their authors will be chronologically exposed.

3.2.1 Fuller

As a great exponent of this area of the structures in that years can be cited R. Buckminster Fuller, who develops his first patent of geodesic dome "Building construction" in 1951 [11], and where can be found a knot with a ball-like cuff configuration. The pieces are held together by means of a bolt, with a coil spring being provided to provide a certain amount of elasticity in the fixation, which is particularly useful during the erection of the structure (Figure 27).
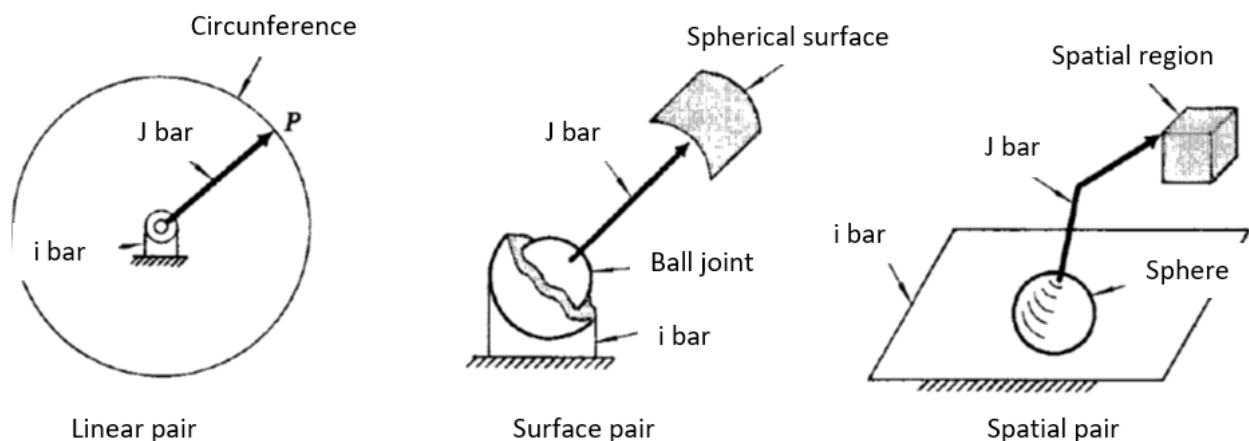
Figure 24. Classification of kinematic torques, Nieto (1978) [9]
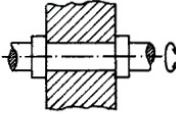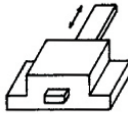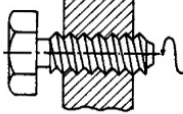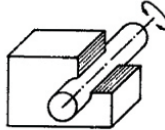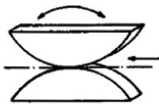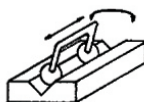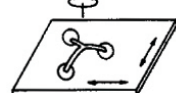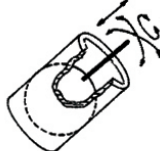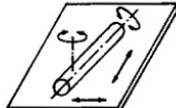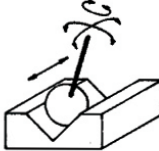
Clase	Grados de libertad	Esquemas, nombres y símbolos de pares cinemáticos			
I	1	Par de revolución R	Par prismático P	Par helicoidal H	Contacto pentapuntual
II	2	Par cilíndrico C	Par esférico ranurado E_r	Par de leva L	Contacto tetrapuntual
III	3	Par esférico E	Par plano P_l	Par cilíndrico ranurado C_r	Contacto tripuntual
IV	4	Par esfera cilindro E_c	Par plano cilindro P_c	Contacto bipuntual	
V	5	Par esfera plano E_p	Par esfera esfera E_e		

Figure 25. Classification of kinematic torques according to the number of degrees of freedom, Nieto (1978) [9]
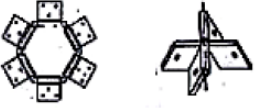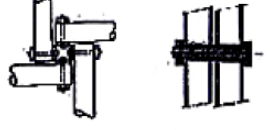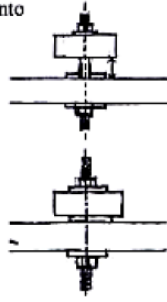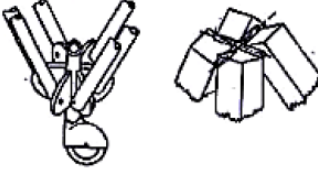
Figure 26. Classification of the transformable structures knots, Rodríguez (2005) [10]
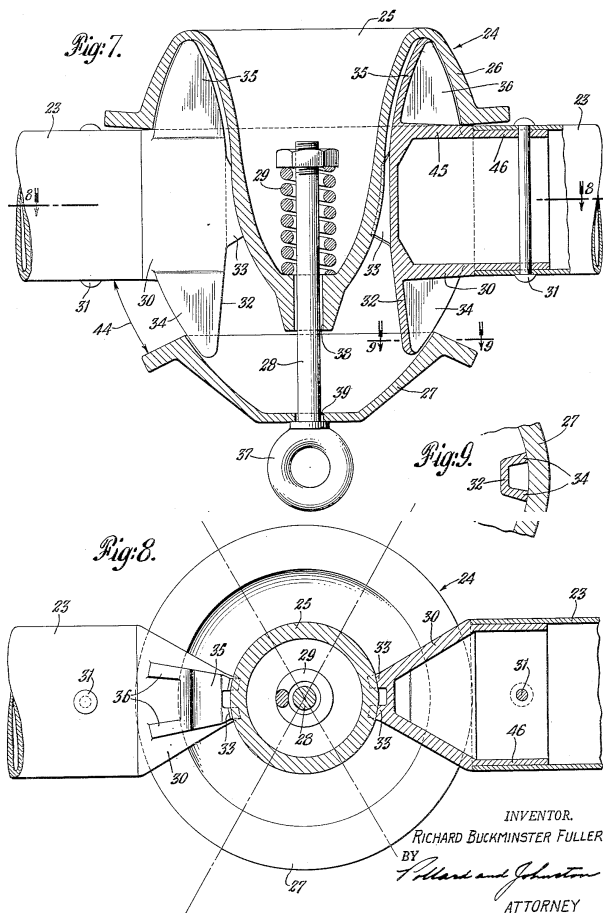
Figure 27. Knot of the geodesic dome "Building construction" (Fuller, 1951) [11]

In 1953 Fuller designed a tripod for their geodesic domes connected by hinged knots and called the Flying Seedpot (Figure 28). This project was realized together with his students with the objective of developing a house capable of being transported on the nose of a space shuttle and being automatically deployed on the lunar surface in 45 seconds. This project was never patented [12].

Figure 28. Flying Seedpot (Fuller, 1953) [12]

3.2.2 Pérez Piñero

In 1961 Pérez Piñero presents his design of a reticular dome that is deployed being completely prefabricated in his patent ES-0266801_A1 [13]. Emilio Pérez Piñero couples three sliding bars in an intermediate node (Figure 29).
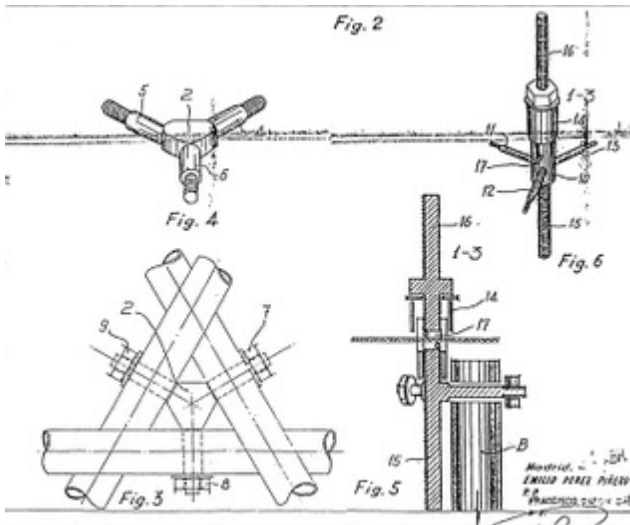
Figure 29. Knot of the patent ES-0266801_A1, Emilio Pérez Piñero (1961) [13]

3.2.3 Albert Moore

Later, in 1967, Albert Moore patented a system of dome called "Pre-assembled structural framework" [14]. It consists of a double curvature triangulated vault with a knot formed by a ring where all the bars reach (Figure 30).
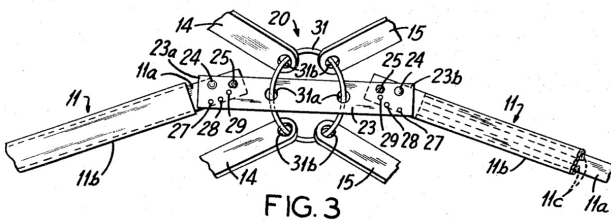
Figure 30. Knot of the patent US3325958, Albert Moore (1967) [14]

3.2.4 Zeigler

In 1977 the patent of Zeigler is published [15], where the points of cross of rod elements crossed in the structure involved may include limited slip connections that affect transfer of contraction force to other cross points that are pivotally attached (Figure 31).

In 1984, based on the Piñero's work, Zeigler patented [16] a self-supporting structure in its deployable form without the need of stiffening elements (Figure 32). The movement is obtained by the used of bolts.
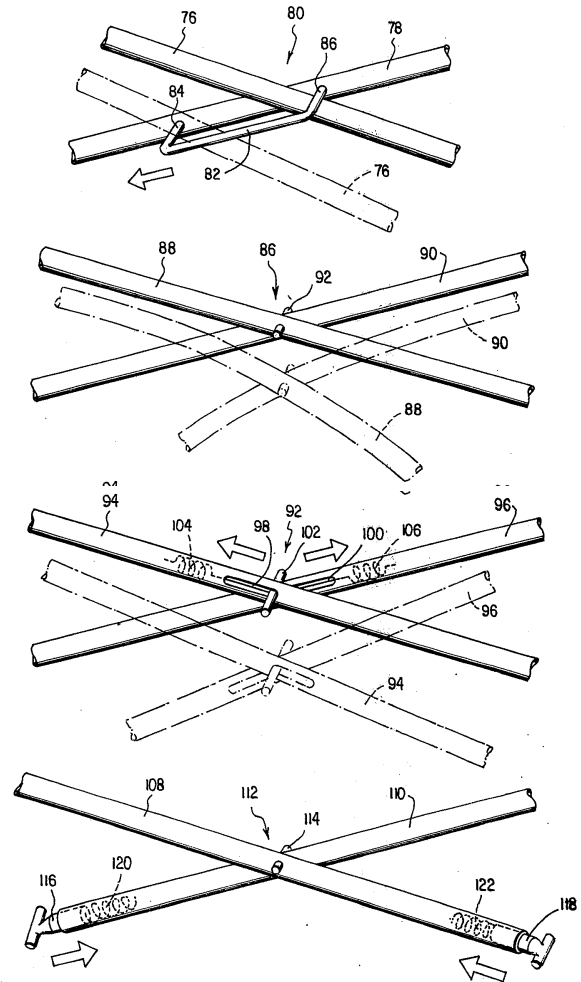
Figure 31. Sliding bar knots, patent US4026313, Zeigler (1977) [15]
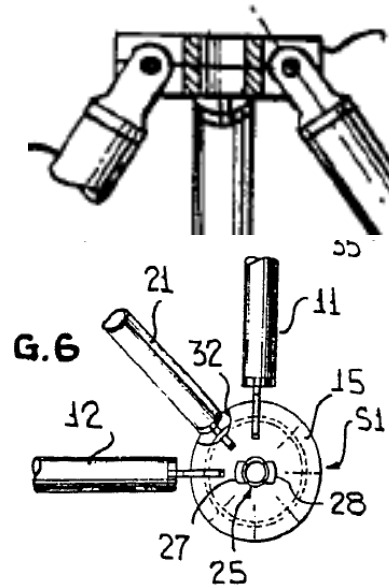
Figure 32. Knot of the patent US4473986A, Zeigler (1984) [16]

3.2.5 Swetish and Baumann

Swetish and Baumann [17] designed some pivoting joints between adjacent support poles for rotation about an axis parallel to the support poles (Figure 33). Each support pole moves between an extended position where the support pole extends perpendicular to the transverse poles and a collapsed position where the support pole extends along the transverse poles.
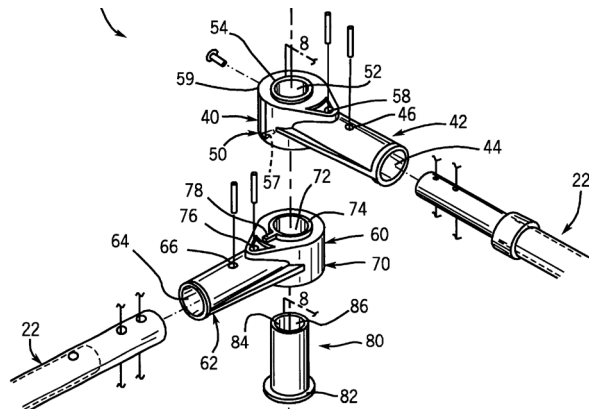
Figure 33. Knot of the patent US 6591849 B1, Swetish and Baumann (2003) [17]

3.2.6 Daniel S-H Lee, Olga Popovic Larsen and Seung-Deog Kim

Daniel S-H Lee, Olga Popovic Larsen and Seung-Deog Kim [18] developed a knot with two hinged connections that allow horizontal and vertical rotation (Figure 34).
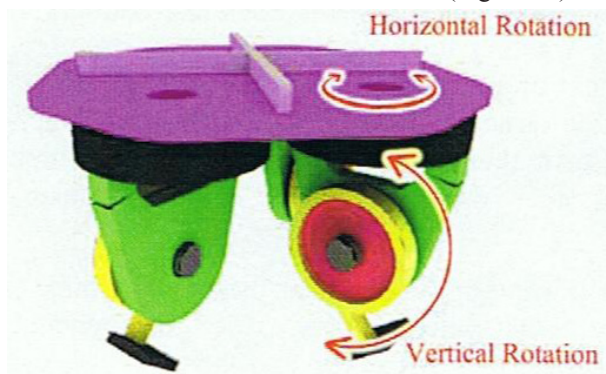
Figure 34. Knot designed and built by Semyung University [18]

3.2.7 SeungDeog KIM, SunKyeong PARK, JePil JANG, InA SIN, JangBog LEE, ChangWoo HA and SeungTeak JUNG

SeungDeog KIM, SunKyeong PARK, JePil JANG, InA SIN, JangBog LEE, ChangWoo HA and SeungTeak JUNG [19] studied cases of articulations and axis that have been developed previously to deployable structures. They suggested new joints and axis with hinges from models (Figure 35).

Figure 35. Mockup knot for test model, SeungDeog KIM et al. [19]

3.2.8 Yohei Yokosuka and Teruo Matsuzawa

An evolution of the rigid spherical knots is the "multi-joint spherical articulation" of Yohei Yokosuka and Teruo Matsuzawa [20]. It is a novel assembled mechanism that permits the tri-axial rotation of the members (Figure 36).
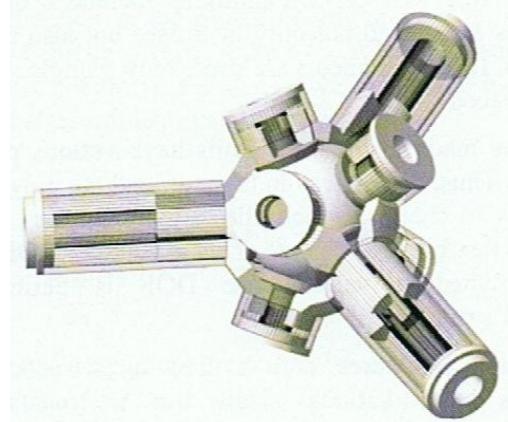
Figure 36. Multi-joint spherical articulation, Yohei Yokosuka and Teruo Matsuzawa [20]

3.2.9 Jesús Anaya, Mª Dolores Álvarez and Ramón Serrano

Jesús Anaya, Mª Dolores Álvarez and Ramón Serrano [21] developed a node called "Octopus" whose configuration allows it to adapt to all the movement configurations of the lattice structure, from simple solutions for the assembly of a flat structure or more complex solutions that even allow the assembly of curved spatial structures or with different angles, all with a single

connecting piece, considerably reducing the price and standardization compared to current solutions (Figure 37).
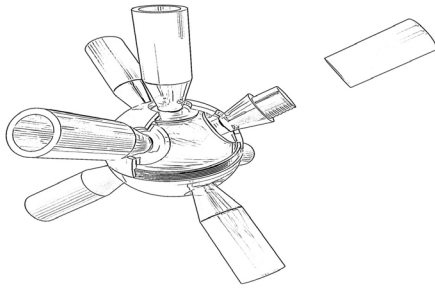
Figure 37. Octopus knot, Jesús Anaya, Mª Dolores Álvarez and Ramón Serrano [21]

4. Comparison of Knot Types Used by Transformable and Rigid Linear Structural Systems

In this apart a new classification about knots is done. In this classification not only the articulated knots are analyzed, like Rodríguez [10] did. Knots types used by transformable and rigid linear structural systems will be analyzed in a same comparison. The classification is represented in Figure 38.

Classification of the knot system	Knot system	Union
Rigid knots structural systems	SDC	Welded
	Pyramitec	Screws
	Tridimatec	Beams in meshes
	Unibat	Board of pyramids and squares
	Spherobat	Hollow sides with screws
	Trio-detic	Bars planes in their ends that are introduced by pressure in serrated grooves that exist in the knots
	Makowski	Pins
	Segmo	Welded
	Tubaccord	Welded or fixed by means of pins
	Bourquardez	Riveting
	Begue	Screws
	Chamayou	Clamps
	Begue-kieffer	Hidraulic group / Slots
	Delacrix-glotin-monier-sejournet	Rivets Welding / Pins
	Kieffer	Welded
	Sarton	Fixing thread
	Spherical	Welded
	Bi-tubular	Welded
	Tesep	Welded / Screwed ribs welded at their ends
	Unistrut	Pins
	Mero	Screwed
	Wupperman	Screwed

	Knot of the geodesic dome "Building construction"	Bolt
Transformable structural systems	Flying Seedpot	Hinges
	Pérez Piñero	Sliding bars
	Preassambled structural framework	Ring to which all the bars reach
	Sliding bar knots (US4026313)	Cross and pivotally
	US4473986A	Bolt
	US 6591849 B1	Pivoting
	Daniel S-H Lee, Olga Popovic Larsen and Seung-Deog Kim	two hinged connections
	SeungDeog KIM, SunKyeong PARK, JePil JANG, InA SIN, JangBog LEE, ChangWoo HA and SeungTeak JUNG	Hinges
	Multi-joint spherical articulation	Assembled
	Octopus	Assembled

Figure 38. Classification of the transformable and rigid linear structural systems knots, own elaboration

Different type of unions appears in different colors in this classification:

Red: knots with screws in their unions, independently if they are rigid or transformable systems.

Blue: knots with welded unions. They are always rigid systems.

Green: other types of unions in rigid systems.

Orange: knots with hinged unions. They are always transformable systems.

Yellow: knots with sliding unions. They are always transformable systems.

Violet: knots with assembled unions. They are always transformable systems.

5. Discussion and Critique of the Analyzed Constructive Systems

As shown in Figure 38, the knot systems can be classified by their unions. This way, we can obtain a series of advantages and disadvantages and utilities of every one of these systems.

Knots with screws in their unions (red) can be used in rigid and transformable systems. They are useful for prefabricated structures that can be assembled on site, because they have the advantage that the assembly is easy. The structure can be disassembled, transported and assembled again in another place.

Knots with welded unions (blue) are always used in rigid systems. They have the disadvantage that they need skilled labor for welding. When the structure is assembled they cannot be disassembled to assemble again in another place. So, it is a permanent structure.

Other types of unions in rigid systems (green) are assembled by pressure, riveting, clamps… They are economic systems and easy to transport. They can be disassembled, but if it occurs generally we have to replace the union system.

Knots with hinged unions (orange) are always for transformable systems. They really have the same advantages and disadvantages that the screwed unions (red). They are easy to assemble on site, and the structure can be disassembled, transported and assembled again in another place.

Knots with sliding unions (yellow) are always for transformable systems. They have the advantage that they are knots completely prefabricated. The disadvantage is the transport, because they are assembled before being loaded.

Knots with assembled unions (violet) are always for transformable systems. They have the advantage that they can be assembled on site, but the assembly is not easy and they need skilled labor to assemble them.

6. Conclusions

A rigid knot is the type of knot that avoids turns and displacements of the elements; it has a particular and immobile configuration. The articulated and slip knots are the type of knots that permit turns and displacements of the elements. They have a particular and mobile configuration.

Architects and designers have looked for flexible systems where joining the bars in different positions in order to employ the knot for more than one configuration is possible. This way, there is a lot of work to do in order to obtain the appropriate knot to some configurations.

In the investigation, a classification of these types of knot based on their union systems has been done. The advantages and disadvantages are considered. Apart from this, a very exhaustive investigation in materials must be done as future prospect, because materials have to absorb the structural efforts in the most solicited structure parts.

So, it is concluded that there are some patents about rigid, articulated and slip knots, but the investigation has to be continued.

Data Availability

No data, models, or code were generated or used during the study.

Conflict of Interest

There is no conflict of interest.

References

[1] MediaWiki., 2006. Construction encyclopedia. http://www.construmatica.com/construpedia. (Accessed 10 May 2022).

[2] Motro, R., 2013. Nodes and Structures-A tribute to Stéphane Du Château. (IASS) Symposium 2013 Beyond the limits of man. Wroclaw, Poland. pp. 8. (in English)

[3] Estrela, C., 2014. The innovative structural conception in Stéphane du Château's work: from metallic trusses to the development of spatial frames. Architectus. 4(40), 51-64. (in English)

[4] Chilton, J., 2000. Space Grid Structures (First ed.). Oxford, England: British Library Cataloguing. pp. 1-180.

[5] Makowski, Z., 2002. Development of jointing systems for modular prefabricated steel space structures. Paper presented at the Proceedings of the international symposium. Warsaw, Poland.

[6] Fentiman, A.E., 1959. Structural framework. US2931467A (Patent). https://patents.google.com/patent/US2931467. (Accessed 10 May 2022)

[7] Carracedo, J., 2005. Knot for reticular structures. WO 2006097545 A1 (Patent). https://patents.google.com/patent/WO2006097545A1/es?oq=Carracedo%2c+J.%2c+2005.+Patent+WO+2006097545+A1 (Accessed 10 May 2022)

[8] Vedoya, D.E., Prat, E.S., 2009. Large Span Structures. Technology and design. ITDAHu editions. pp. 1-243.

[9] Nieto, J., 1978. Synthesis of mechanisms. AC Publishing, Madrid. pp. 1-206.

[10] Rodríguez, N., 2005. Design of a structure that can be transformed by deformation of a flat mesh in its application to a quick-assembly shelter. Thesis of Polytechnic University of Catalunya, High Technique School of Architecture of Barcelona, Barcelona. pp. 1-297.

[11] Fuller, R.B., 1951. Building construction. US 2682235A (Patent). https://patents.google.com/patent/US2682235A/en?oq=Fuller%2c+R.B.+Building+construction.+US+2682235+(Patent)+1951. (Accessed 10 May 2022)

[12] Fuller, R.B., 1953. Flying Seedpot. Geodesic Dome Project, Washington University and Fuller Research Foundation, St. Louis https://www.bfi.org/about-fuller/resources/everything-i-know/session-11 (Accessed 10 May 2022)

[13] Pérez, E., 1961. Foldable stereo lattice structure. ES0266801 A1 (Spanish Patent). 3.185.164 (US Patent).

[14] Moore, A., 1967. Preassambled structural framework. US3325958 (Patent).

[15] Zeigler, T.R., 1977. Collapsible self-supporting structures. US4026313 (Patent).

[16] Zeigler, T.R., 1984. Collapsible/expandable structural module with split hub locking. US4473986A (Patent).

[17] Thomas, R., Swetish, T.R., Baumann, W.R., 2003. Foldable frame structure. US 6591849 B1 (Patent).

[18] Lee, D.S.H., Popovic, O., Kim, S.D., 2013. Study of the connection joint for scissor-type deployable structure for the possible application in emergency evacuation shelter. New proposals for transformable architecture, engineering and design. Ed. STAR-BOOKS Structural Architecture. pp. 105-109.

[19] Kim, S.D., D., Park, S.K., Jang, J.P., et al., 2013. A Study on Deployable Shelters Considering Biaxial Rotations of Joints. New proposals for transformable architecture, engineering and design. Ed. STAR-BOOKS Structural Architecture. pp. 111-114.

[20] Yokosuka, Y., Matsuzawa, T., 2013. Shape-finding Analysis for Variable Geometry Structures Formed by a Multilink Spherical Joint. New proposals for transformable architecture, engineering and design. Ed. STARBOOKS Structural Architecture. pp. 83-88.

[21] Anaya, J., Álvarez, M.D., Serrano, R., 2020. Union system for mobile reticular structures. ES 1238524 Y (presented Spanish patent). U. 201931716 (8) (utility Spanish model).

ARTICLE

A Comparative Study between Pseudo-static and Dynamic Analyses of Keddara Dam

Manish Sharma[*] ID   Md. Imteyaz Ansari ID   Nazrul Islam ID

Department of Civil Engineering, Faculty of Engineering and Technology, Jamia Millia Islamia, New Delhi, Delhi, 110025, India

ARTICLE INFO	ABSTRACT
	The numerical analysis of static and dynamic performance of embankment dams using the finite difference approach is a complex procedure that takes into account material behavior, soil-dam foundation interaction, hydraulic conditions, and saturation effects. In this study, a numerical analysis using the finite difference method (FLAC 3D) is used to conduct a static and dynamic analysis of the Keddara earthen dam in the Boumerdes region of Algeria, with the goal of defining its behaviour in terms of settlement, deformation, and pore pressure variation during construction and operation. There are two steps to consider: dam construction and water filling. For the static analysis, two mathematical models are considered: the elastic model and the Mohr-Coulomb model. An actual earthquake record is used to conduct a coupled dynamic analysis, and the interaction between the fluid and solid phases is taken into account. Maximum displacement, acceleration, and pore pressure remain inconsequential for dam instability; horizontal and vertical displacements increase with distance from the dam body's base to the top.

1. Introduction

Embankment dams are major water impoundment facilities. They are most likely the earliest man-made hydraulic structures. They are dams that are built with natural materials mined locally. Earthfill or rockfill dams are the most common types. The various structure sections of an earth dam contain a variety of materials. Earth dams are generally prone to displacement during construction, following water filling, and during operation [1-3]. Earth dams are extremely vulnerable to seismic response issues, and earthquake loading can result in severe consequences ranging from economy to direct loss of life.

The ancient method and seismic criteria were used to design the old earth dam. The safety of these structures is now jeopardised due to noncompliance with current seismic safety recommendations [4,22]. Dams should operate without endangering the population in the event

Corresponding Author:
Manish Sharma,
Department of Civil Engineering, Faculty of Engineering and Technology, Jamia Millia Islamia, New Delhi, Delhi, 110025, India;
Email: manish164300@st.jmi.ac.in

of an earthquake, and similarly under static loading. As a result, the stability of dam embankments, whether static or dynamic, remains a major concern for geotechnical engineers. Dam security is related to the strength of the dam body and foundation, permanent deformation generating cracks, slope stability, excess pore water pressure in embankments, and foundation materials [5]. According to a literature assessment, the most common causes of earth dam collapses are overtopping and internal erosion [6]. Significant progress has been made in understanding dam behaviour, particularly during seismic action. The development of numerical techniques for static and dynamic analysis was largely responsible for the progress [7].

Different methods can be used to analyse the stability of embankments and earthen dams subjected to seismic loads [23]. The methodologies have advanced greatly in recent years, and they range from simplified to detailed. Gazetas (1987) [8] compared techniques for calculating the seismic response of earthen dams subjected to seismic action and defined their advantages and limitations. Simplest approaches require few parameters for the analysis and are based on empirical correlations and simpler procedures. Solutions in decoupled linear-equivalent analysis, as well as finite element and finite difference formulations in coupled or decoupled nonlinear analysis [9,4], are detailed analyses. Simplified approaches are used to analyse small dams or to justify the use of extensive analysis for major dams. The pseudo – static method was widely utilized to assess the seismic stability of embankment dams. This method reduces the dynamic behavior to static forces. It involves replacing the seismic action with a single force and calculating the factor of safety for the sliding block that is limited by the critical failure plane. Simultaneously, the shear beam technique proved to be efficient in dynamic analysis. The approach took into account earthquake vibrations in several directions, including transverse, vertical, and longitudinal [8,10]. For additional analysis, analogous linear or non-linear analyses are used [11].

The goal of this research is to use a numerical method to examine the static and seismic response of the Keddara dam in Algeria. The analysis focuses on the effect of the mathematical model on the static analysis response of the dam during the building phase and water filling phase. The elastic model and the Mohr-Coulomb model are used in the analysis. First, the elastic model is used for the foundation and the Mohr-Coulomb model for the dam body (model (1)). Second, for both the foundation and the dam body (model (2)), the analysis is carried out using the Mohr-Coulomb model. Finite difference formulations in coupled nonlinear analysis are used for the dynamic analysis during the water filling phase. The obtained displacements, deformation, and pore pressure evolution data are discussed.

2. Description of Keddara Dam

The Keddara dam is a rockfill embankment built between 1982 to 1985. It is situated in the Boumerdes region, approximately 35 kilometers east of Algiers. The site is located in the Tellian Atlas coastal range, at 36.65° North latitude and 3.43° East longitude, near the northern edge of the Mitidjian Atlas. This dam has a capacity of 142.39 million cubic meters and a height of 108 meters. Figures 1 and 2 depict the dam's geometry and position, respectively.
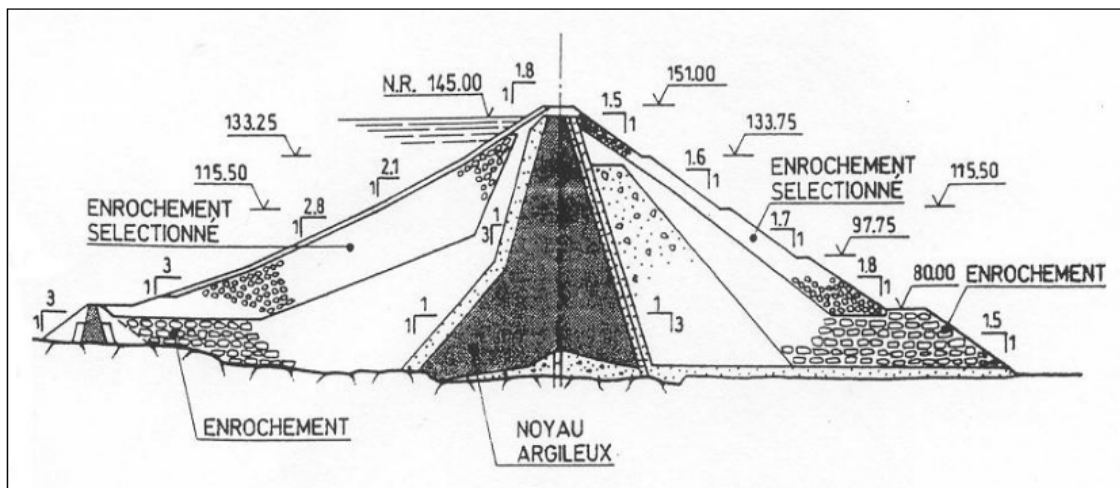
Figure 1. Geometry of Keddara dam (ANB 1987) [12].

Based on site investigations, the geotechnical parameters were obtained [12]. As shown in Table 1, and Figure 3, materials of the dam have been subdivided into six zones. The upstream part consists of limestone rockfill (Zone 1) and a transition filter (Zone 2). The downstream part consists of limestone rockfill (Zone 1), a sand filter (Zone 4) and a gravel backfill (Zone 5) and in the center clayey soil as core materials (Zone 3). The foundation of the dam is composed of stiff schist materials (Zone 6). The characteristics of materials in each zone of the dam are summarized in Table 1, where γ_d is the dry density, c' is the effective cohesion, υ' is the effective angle of internal friction, G is the shear modulus and K is the bulk modulus.
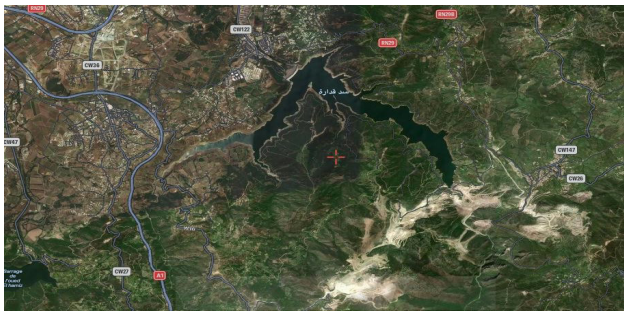
Figure 2. Location of Keddara dam on the Boudouaou River in Boumerdès Province, Algeria. (Captured by satellite pro).
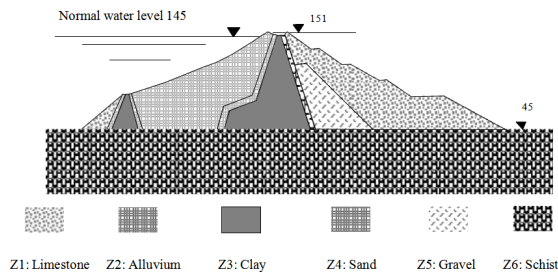
Figure 3. Different zones of the dam.

3. Numerical Modeling

The dam analysis is conducted using the finite difference program FLAC-3D, based on a continuum finite difference discretization using the Lagrangian approach. FLAC (Fast Lagrangian Analysis of Continua) [13], was developed by ITASCA group, to solve geotechnical problems. As reported in the manual program: "Every derivative in the set of governing equations is replaced directly by an algebraic expression written in terms of the field variables (e.g. stress or displacement) at discrete point in space. For dynamic analysis, it uses an explicit finite difference scheme to solve the full equation of motion using lumped grid point masses derived from the real density surrounding zone". Figure 4 shows the three-dimensional mesh used for the Keddara dam analysis consisted of 1235961 elements.
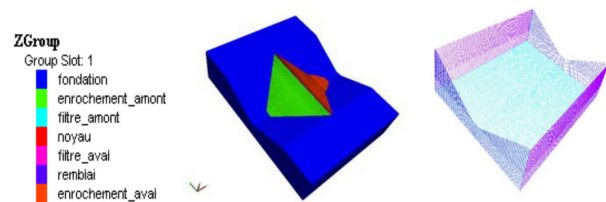
Figure 4. 3D Modeling of Keddara dam and Boundary Condition

The construction of the dam embankment is modeled layer by layer with a same thickness, starting from the upstream side to the downstream side, and up to the crest (151 NGA). The first embankment layer is modeled after foundation analysis (equilibrium state). The appropriate boundary conditions in modeling and grid were selected according to the FLAC3D manual program guidelines. Boundary conditions are imposed along the lateral borders and the base of the model, such as the displacements are zero, and the nodes on the foundation external surface are fixed on the three directions X, Y, Z.

Mohr-Coulomb plasticity model is used for sandy

Table 1. Geotechnical Soils Properties [15]

Zones		Materials	γ_d [kN/m³]	c' [kPa]	υ'[°]	K [MPa]	G [MPa]
Zone 1	Rockfill	Selected limestone	25	0	45	9.6×10^6	5.8×10^6
Zone 2	Transition filter	Alluviums	18	50	13	260×10^3	120×10^3
Zone 3	Core	Colluvial clay	20	55	14	253.5×10^3	117×10^3
Zone 4	Drain	Sand	18	0	35	433.3×10^3	200×10^3
Zone 5	Backfill	Gravel materials	18	0	40	274.67×10^3	160×10^3
Zone 6	Foundation	Schist	28	0	45	2.67×10^7	1.6×10^7

and clayey materials that yield when subjected to shear loading. The criterion depends on minor and major principal stresses as presented in Equation (1).

$$F(\sigma'_{ij}) = |\sigma'_1 - \sigma'_3| - (\sigma'_1 + \sigma'_3)sin\varphi' - 2c'cos\varphi' = 0. \quad (1)$$

σ'_1 and σ'_3 are the principal stresses and υ is the angle of internal friction.

Mechanical parameters of Mohr-Coulomb criterion are: E (Young's Modulus), υ (Poisson ratio), c (cohesion), υ (angle of internal friction) et ψ (dilatancy angle). Mohr-Coulomb model parameters are obtained from laboratory tests. C and φ are calculated in the Mohr plane (σ, τ) using the stress states at failure.

The shear strength equation for saturated soils is expressed as a linear function of effective stress as:

$$r = c' + (\sigma - u)tg\ \varphi'. \quad (2)$$

c' is the effective cohesion, υ' is the effective angle of internal friction, σ is the total normal stress in the plan of failure, and *u* is the pore water pressure.

In FLAC 3D, the Mohr-Coulomb model is the conventional model used to represent shear failure in soils. The model is expressed in terms of the principal stresses (s_1, s_2, s_3), which are the three components of the generalized stress vector of this model. The components of the generalized strain vector are the principal strains e_1, e_2 and e_3. The increment expression of Hooke's law in terms of the generalized stress and stress increments has the form [13,24,25]:

$$\begin{cases} d\sigma_1 = \alpha_1 d\varepsilon_1 + \alpha_2(d\varepsilon_2 + d\varepsilon_3) \\ d\sigma_2 = \alpha_1 d\varepsilon_2 + \alpha_2(d\varepsilon_1 + d\varepsilon_3) \\ d\sigma_3 = \alpha_1 d\varepsilon_3 + \alpha_2(d\varepsilon_1 + d\varepsilon_2) \end{cases} \quad (3)$$

where $\alpha_1 = K + 4G/3$, $\alpha_2 = K - 2G/3$. a_1 and a_2 are the material constants defined in terms of the shear modulus G and bulk modulus K.

For rockfill dams, it is recommended to consider an average shear modulus, function of the depth of the dam from the crest [14,8]:

$$G(z) = G_b \left(\frac{Z}{H}\right)^m \quad (4)$$

G_b is the average shear modulus at the base. According to Gazetas (1987) [8] m is taken equal to 2/3. Noting that different formulas were used to determine the shear modulus according to the type and density of materials [15,16,24].

In the construction stage, the analysis is conducted using the elastic model for the foundation and Mohr-Coulomb model for the dam body (model (1)). Therefore, the linear elastic law (Hooke's law) is used considering the mechanical properties; Young's Modulus E and Poisson ratio υ. Due to the nature of the body dam materials, the elastoplastic Mohr-Coulomb model is used. In this model, the behavior is assumed first elastic and then plastic. In

addition to the elastic deformation defined by Hooke's law, the elastoplastic models integrate a permanent plastic deformation.

4. Dynamic Analysis

The research is carried out with the 2003 Boumerdes earthquake record in order to examine the dam response to real earthquake action. The Boumerdes earthquake, with a magnitude of Mw = 6.8 and an intensity of I = X, killed around 2000 people and injured 11,000 others [17]. According to the Algerian Research Center of Astronomy, Astrophysics, and Geophysics, the epicentre was located around 20 kilometres from the Keddara dam at 36.91° N and 3.58° E, at a depth of 8 kilometres to 10 kilometres (CRAAG).

The Boumerdes earthquake had a peak acceleration of 0.202 g and a length of around 30 seconds. Figure 5 depicts the record. The frequency of the primary peak is 13.3 Hz, as illustrated in Figure 5. The Mohr-Coulomb creteri on is used to undertake the dam's elastoplastic analysis for both the dam core and the foundation (model (2)). The analysis performed is a comprehensive coupled analysis that takes into account effective stresses, an anisotropic fluid model for the core, and an isotropic model for the dam's other materials. The interaction between the fluid and solid phases is considered in the study. The main objective is to investigate the influence of water filling on the dam response to real earthquake, and to compare the numerical results to the real behavior of the dam to the 2003 earthquake.

Except for the foundation, the water flow in the dam is taken into account when doing a coupled analysis. As a result, the core permeability is taken to be k1 =1.10~12 m/s, k2 =1.10~12 m/s, and k3 =1.10~13 m/s in the directions x, y, and z, with the porosity n=0.8.

5. Results and Discussions

5.1 Vertical Displacement

The numerical analysis allows for the measurement of vertical dam displacement during construction and after water filling. According to the two models (1) and (2), vertical displacement in the dam at the conclusion of the construction stage and before water filling is shown in Figures 6 and 7. The dam core is where the most settlement is induced (Zone 3). Despite the comparable distribution of settlements across models (1) and (2), model (l) (Elastic for the foundation and Mohr-Coulomb for the dam body) has a bigger induced settlement of 9.44 cm compared to 8.86 cm for model (2). (Mohr-Coulomb

for the foundation and the dam). However, according to Figure 8, the displacement variation with the dam axis shows an increase of displacement at the top with 22 cm and 20 cm respectively for the models (1) and (2). Figure 8(a)-(b) shows that the induced settlements variation, according to models (1) and (2), with the dam axis, in stage of construction and after water filling, is no significant. A slight variation is noted in the middle (h/H = 0.5) and the top (h/H = 1) of the dam.

Figure 7. Settlement [m] of the Dam According to Model (2)

(a)

(b)

Figure 5. (a) Boumerdes Earthquake Record (b) Fourrier Spectra

(a)

(b)
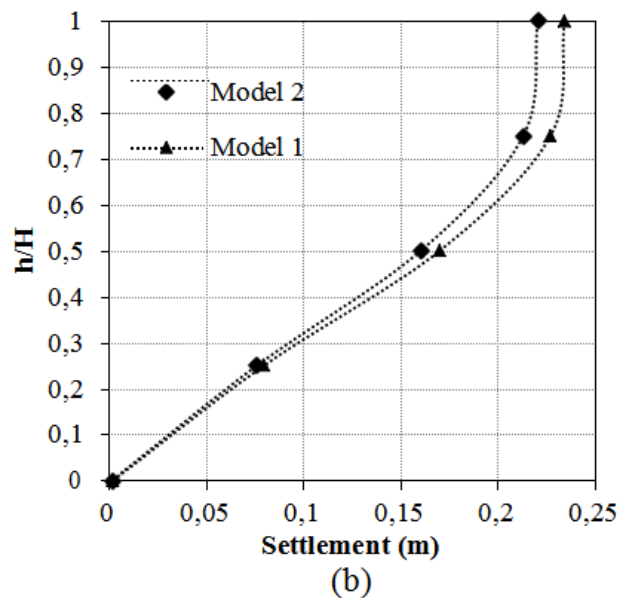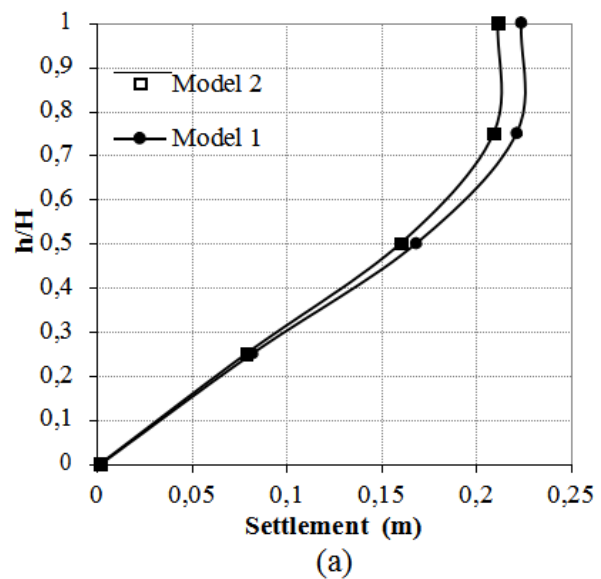
Figure 8. Comparison of settlements with the dam axis according to model (1) and Model (2) (a) before water filling, (b) after water filling.

Figure 6. Settlement [m] of the Dam According to Model (1)

5.2 Comparison with Settlements Recorded on Site

The dam filling water began by the end of 1985. Using dam tools instrumentation for data monitoring consisted of magnetic inclinometers/taseometers (listed from 1 DZ to 12 DZ as shown in the legend of Figure 9), fixed at the top of the dam, on the core and the downstream and upstream recharge, settlements and deformation of the structure were recorded. The crest settlement histories, between 1987 and 2004, are presented in Figure 9(a)-(b) [18]. The cumulative settlements in the period have reached 450 mm in the middle of the backfill, with a rate of around 15 mm/year. It should be noted a differential settlement of around 150 mm between the upstream and downstream marks of the right bank profile. The cumulative settlement has reached about 6 mm per m of backfill since 1987.

(a)

(b)
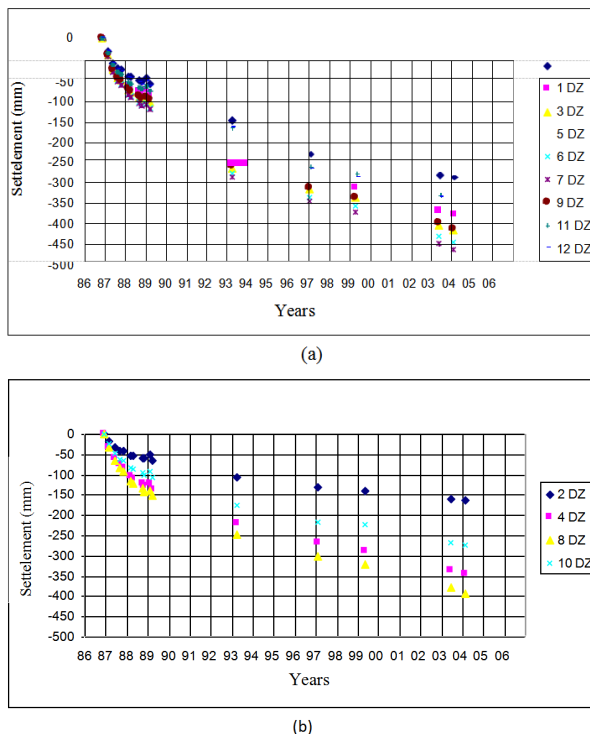
Figure 9. Settlement at the Crest of the dam from 1987 to 2004; (a)Upstream Mark, (b) Downstream Mark (ANB 2006)

5.3 Deformations

Considering the two stages, before and after water filling, and using the two models (1) and (2), the dam response in terms of deformation is presented in Figure 10 and Figure 11. It shows an increase in deformation with the dam axis. The deformation variation in XY and YZ directions seems to be low, with an insignificant increase value at the top of the dam. Deformation is negligible in the other directions of the structure.

(a)

(b)
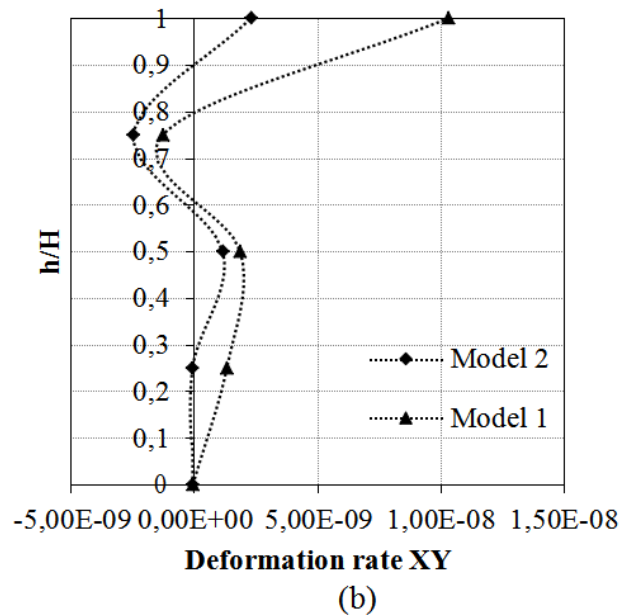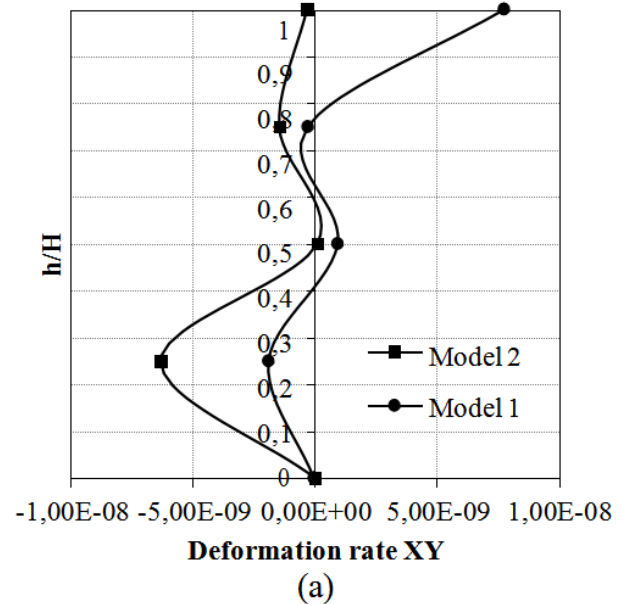
Figure 10. Dam deformation considering Model (1) and (2) in XY Direction

5.4 Pores Pressure Variation

The variation in pore pressures with the dam axis (base, middle and top) in the dam core and the upstream rockfill, accordingly to the models (1) and (2) (Figure 12(a)-(b)). Pore pressure is more important at the base of the dam body and decreases with the dam axis. We can see identical values of pressure in the dam core and the rockfill for model (1). However, for model (2), the pore pressure varies according to the nature of the material (core or rockfill).
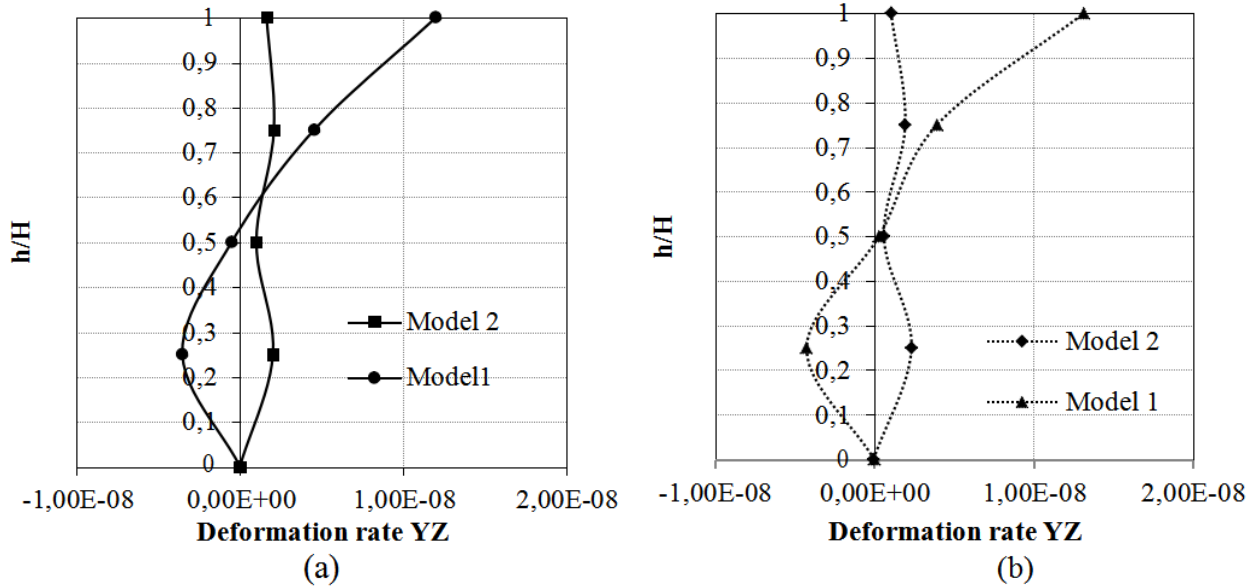
Figure 11. Dam deformation considering Model (1) and (2) in YZ direction
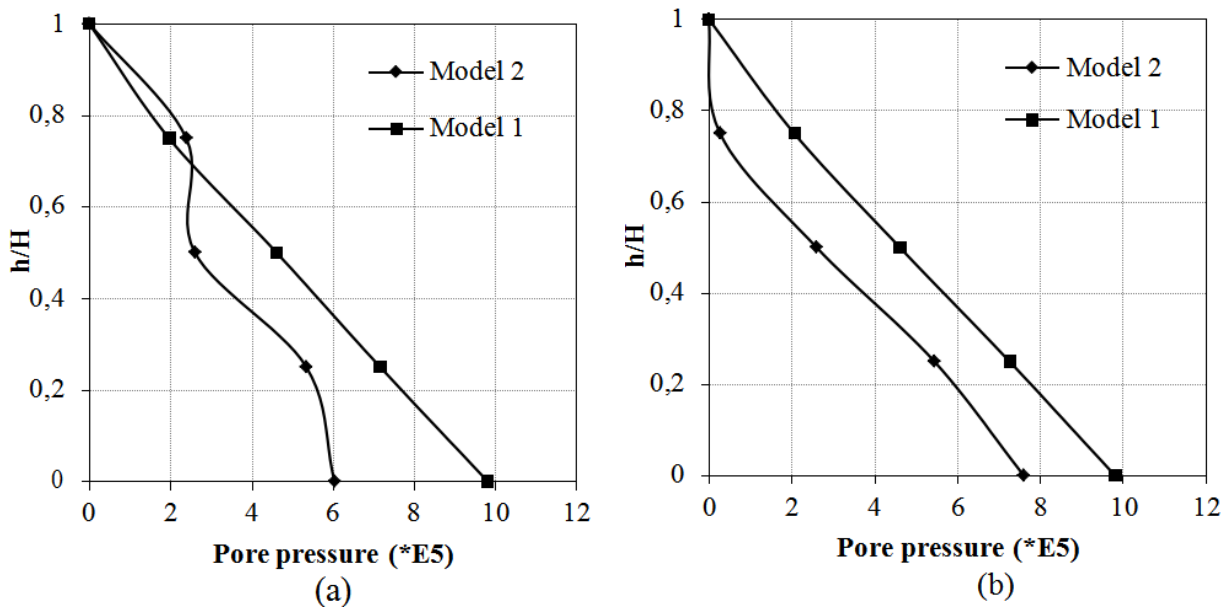
Figure 12. Pores pressure variation in the dam for the two Models (a) Core (b) Upstream rockfill

5.5 Dynamic Analysis Response

The coupled analysis concerns the response of the dam to the Boumerdes 2003 earthquake record. Geotechnical properties are summarized in Table 1. The foundation is assumed to be stiff with a Young's Modulus E= 4.10^7 MPa and the permeability and porosity of the core are equal to 1.10^{-12} m/s and n=0.8.

The seismic loading induces a maximum displacement in the seismic excitation X-direction at the dam core and downstream rockfill, which attains 10.4 cm (Figure 13). We can see the displacement variation with the dam axis (base, middle and top) under the maximum of the seismic

excitation. The displacement increases with the distance from the base of the dam body with an approximative stabilization in the middle and the top of the dam. Figure 14 shows the maximum vertical displacement under the earthquake, which correspond to a very slight increase at the top of the dam, but remains insignificant [5,19,20]. It is worth noting that the permanent static vertical displacement is not considered in dynamic response. Figure 15 shows the induced acceleration in the dam under the seismic excitation. It can be observed a quasi-stabilization of the acceleration from the base to the top of the dam, except at the middle of the core where it

increases. Figure 16 provides the pore pressure evolution in the dam under seismic loading. It can be observed that the seismic excitation induces an increase in the pore pressure in the base of the dam body, with an excess pore pressure ratio of 1.14 compared the static state [5,21]. This increase remains not significant to produce liquefaction or instability of the dam. The impermeable clay core has oriented to the upstream face, which indicates more stability.

Finally, it was observed that the core clay affected the dam behaviour under earthquake effect. It was noted that the dissipation of the pore pressure is fast during and after construction due to increasing of stresses and settlement at the end of construction.
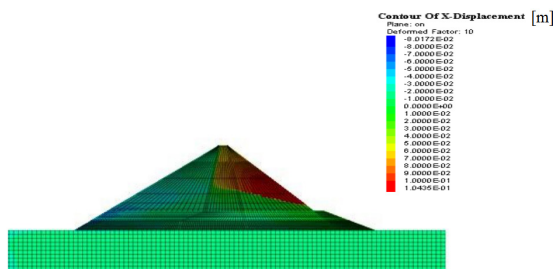
Figure 13. Dam displacement in the X direction under seismic loading
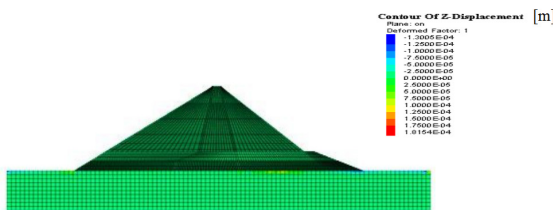
Figure 14. Dam displacement in the Z direction under seismic loading
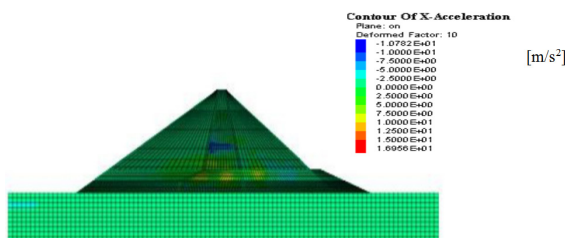
Figure 15. Dam acceleration [m/s²] in the X direction under seismic loading
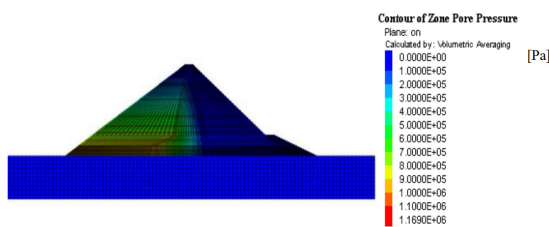
Figure 16. Pore pressure variation [Pa] in the dam under seismic loading

6. Conclusions

This paper presents the static and seismic examinations of earth dam utilizing finite difference method. Mathematical examination of the Keddara dam, situated in Boumerdes district (Algeria), is directed utilizing FLAC 3D program, with the target to characterize its static and dynamic way of behaving, as far as settlement, distortion and pore pressure variety during its construction and operation .

- The dam's response is described using an elastic model and an elastoplastic constitutive model with the Mohr-Coulomb failure criterion.
- Static study demonstrated that the largest induced settlement is found in the dam core.
- The displacement variation along the dam axis demonstrates an increase in displacement at the dam's top. In the case of vertical displacement, the calculation model has no effect, whereas deformation and pore pressure do. Monitoring data reveals that the dam's static settlement has been completed with the consolidation time.
- Furthermore, pore pressure is greater near the dam body's base and decreases with dam axis.
- The three-dimensional seismic analysis of Keddara dam was conducted using Boumerdes earthquake (2003) record.
- Horizontal and vertical displacements rise with distance from the dam body's base to the top; maximum displacement, acceleration, and pore pressure remain insignificant for dam instability.

Conflict of Interest

There is no conflict of interest.

References

[1] Karalar, M., Cavusli, M., 2019. Examination of 3D long-term viscoplastic behavior of a CFR dam using special material models. Geomechanics and Engineering. Technopress. 17(2), 119-131.
DOI: https://doi.org/10.12989/GAE.2019.17.2.119

[2] Chen, Y., Fry, J.J., Laigle, F., et al., 2012. Numerical Analysis of High CFRD Using an Elastoplastic Constitutive Model International symposium on dams for a changing world.

[3] Chen, Y., Fry, J.J., Laigle, F., et al., 2013. Prediction of large rockfill dam behavior using three-dimensional modeling. Proceedings of the 18th International Conference on Soil Mechanics and Geotechnical Engineering, Paris.

[4] Parish, Y., 2007. Numerical analysis of the seismic

behaviour of earth dams: influence of plasticity and pore water pressure (Doctoral dissertation, PhD Thesis, University of Science and Technology of Lille, France).

[5] Gordan, B., Raja, M.A., Armaghani, D.J., et al., 2021. Review on Dynamic Behaviour of Earth Dam and Embankment During an Earthquake. Geotechnical and Geological Engineering. pp. 1-31.
DOI: https://doi.org/10.1007/s10706-021-01919-4

[6] Jandora, J., Říha, J., 2008. The failure of embankment dams due to overtopping. Brno, Czec Republic: Vutium.

[7] Parish, Y., Abadi, F.N., 2009. Dynamic behaviour of earth dams for variation of earth material stiffness. Proceedings of World Academy of Science: Engineering and Technology. 50, 606-611.

[8] Gazetas, G., 1987. Seismic response of earth dams: some recent developments. Soil Dynamics and Earthquake Engineering. 6(1), 2-47.

[9] G Deraa, M., H Jalut, Q., M Abbas, J., 2019. Numerical Modeling to the Dynamic Response of Mindali Earth Dam. International Journal of Civil Engineering and Technology. 10(8).

[10] Abdel-Ghaffar, A.M., Koh, A.S., 1981. Longitudinal vibration of non-homogeneous earth dams. Earthquake Engineering & Structural Dynamics. 9(3), 279-305.

[11] Seed, H.B., Lee, K.L., Idriss, I.M., et al., 1973. Analysis of the slides in the San Fernando dams during the earthquake of Feb. 9, 1971. College of Engineering, University of California.

[12] National Dam Agency ANB, 1987. Keddara Dam Monograph.

[13] FLAC 3D Itasca, User's and theory manuals of FLAC3D, 2009. Fast Lagrangian analysis of continua in 3D, version 4, Minneapolis, Itasca Consulting Group Inc.

[14] Abdel-Ghaffar, A.M., Scott, R.F., 1979. Shear moduli and damping factors of earth dam. Journal of the Geotechnical Engineering Division. 105(12), 1405-1426.

[15] Louadj, S., Bahar, R., Laouami, N., 2018. Numerical Analysis of Keddara Dam under Seismic Motion. International Journal of Engineering Research in Africa. Trans Tech Publications Ltd. (40), 47-62.

[16] Oner, M., 1984. Shear vibration of inhomogeneous earth dams in rectangular canyons. International Journal of Soil Dynamics and Earthquake Engineering. 3(1), 19-26.

[17] Department of Housing, Public Facilities (DLEP), 2004. Consequence of the earthquake on the housing stock and public facilities, Wilaya de Boumerdes.

[18] National Dams Agency ANB, 2006. Keddara dam auscultation report.

[19] Meziani, F., Kahil, A., Gabi, S., 2019. Evolution of Soil Settlements under a Rockfill Dam Based on Potential Earthquake Harmfulness (PEH) 'Case of Boumerdes Earthquake, Algeria 2003'. International Journal of Engineering Research in Africa. Trans Tech Publications Ltd. (42), 109-121.
DOI: https://doi.org/10.4028/www.scientific.net/JERA.42.109

[20] Mazaheri, A.R., Komasi, M., Veisi, M., et al., 2021. Dynamic analysis of earth dam using numerical method–A Case Study: Doyraj Earth Dam. Acta Geotechnica Slovenica. 18(1), 65-78.

[21] Beiranvand, B., Mazaheri, A.R., Komasi, M., 2021. Quasi-static and dynamic analysis of pore water pressure in Azadi earth dams using Abaqus software. Arabian Journal of Geosciences. 14(13), 1-12.
DOI: https://doi.org/10.1007/s12517-021-07533-1

[22] Bharti, M.K., Sharma, M., Islam, N., 2020. Study on the Dam; Reservoir, and Analysis of Dam Failures: A Data Base Approach. International Research Journal of Engineering and Technology. pp. 1661-1669.
DOI: https://doi.org/10.6084/m9.figshare.19686372

[23] Sharma, M., Ansari, Md.I., 2019. Seismic Response Prediction of Concrete Arch Dam, Seismic Hazard Mitigation of Structures published by Cyber Tech. pp. 307-3014.
DOI: https://doi.org/10.6084/m9.figshare.19686420

[24] Sharma, M., Ansari, M., Islam, N., 2022. Study of Concrete Filled Unplasticized Poly-Vinyl Chloride Tubes as Columns under Axial Loading. Journal of Mechanical Materials and Mechanics Research. 5(1), 10-17.
DOI: https://doi.org/10.30564/jmmmr.v5i1.4494

[25] Rawat, S., Patel, P., Pal, S., et al., 2020. Performance Evaluation of Fiber Reinforced Concrete & Conventional Concrete. International Journal of Innovative Research in Science, Engineering and Technology. 9(5), 3309-3313.
DOI: https://doi.org/10.6084/m9.figshare.19686435

ARTICLE

Evaluation and Effectiveness of Reallocating Traffic Signal Timing at Corridors with High Freight Volume

Ijeoma Ihuoma-Walter[1]* **Celeste Chavis**[2] **Adewole Oladele**[1]

1. Civil Engineering Department, Morgan State University, Baltimore, MD 21251, United States
2. Transportation and Urban Infrastructure Studies, Morgan State University, Baltimore, MD 21251, United States

ABSTRACT

The COVID-19 pandemic drastically altered traffic patterns across the globe. With more people staying at home and relying on delivery services, there was a reduction in passenger car traffic but an increase in freight traffic. This study investigates the changes in traffic volume and mode splits during the COVID-19 pandemic at the intersection of Broening Highway and Holabird Avenues and investigates traffic signal reallocation strategies that account for the changes in traffic. This study considers morning peak traffic volumes before and during COVID. A methodology was developed to evaluate and measure freight volumes and emissions. From the literature, the cost per kilogram of CO, VOC, and NOx was $5.85, $3,37, and $12.53, respectively. The intersection operated at a level of service (LOS) of C both pre-COVID and during COVID. Traffic volume decreased by 24.3% during COVID at the study location; car volumes declined by 50%, and truck volumes increased by 130%. The total rate of emissions decreased by 22.6%.

1. Introduction

The United States is currently experiencing a rise in emerging technology advancement and a shift of businesses to e-commerce. Densely populated urban areas are suddenly becoming aware of these changes and are adopting emerging technology advancements into their daily lives and increasing their inventory of goods online and demanding quick delivery of goods ordered online, often within 24 hours. The COVID-19 pandemic has further fueled e-commerce industries to change their distribution model to support these improvements suddenly. The distribution model improvements are causing an increase in heavy-duty freight trucks on the roadways. Hence, the inclusion of heavy-duty freight truck in traffic signal allocation at intersections to reduce delay is paramount because the exhaust emission released is higher for freight truck during signal delay at the

Corresponding Author:
Ijeoma Ihuoma-Walter,
Civil Engineering Department, Morgan State University, Baltimore, MD 21251, US;
Email: ijihu1@morgan.edu

intersection. Conversely, the demand for transportation and logistics in certain sectors such as e-commerce has surged [1]. Hence, the COVID-19 pandemic has dramatically illustrated the need for transportation professionals to prepare for future disruptions [1]. This research used traffic volumes to evaluate the disruption in traffic volumes and surge in freight traffic volumes and suggest the need to reallocate signal timing in corridors with high volumes of freight truck to reflect changes in COVID and post COVID volumes at intersection due to the surge in heavy-duty freight trucks.

The solution seeks to minimize delay and analyze performance measures for reducing emission at the intersection through traffic signal reallocation. This research focused on the need to reallocate traffic signals that can be applied to any intersection corridor with a high volume of freight truck traffic. Existing data from Maryland State Highway Administration, Maryland Ports Administration and Maryland Transportation Authority. The study area is located at the intersection of Broening Highway and Holabird Avenue in Baltimore, Maryland. An Amazon facility is located along this corridor, contributing to the volume of heavy-duty freight truck traffic.

Study Area

The study area is at the intersection of Holabird Avenue and Broening Highway, located in Baltimore City. The Amazon Fulfilment Center is located along Holabird

Avenue and Broening Highway, as well as other industries. This intersection is one mile from the Port of Baltimore (Figure 1). Study Area shows the study area Holabird Avenue and Broening Highway. The traffic data showed a significant increase of vehicle and truck traffic from 2008-2011 to 2012-2016. The Amazon Fulfillment Center, which opened in 2012, is located on Holabird Avenue in Baltimore, and it operates a 24 hours' freight services. Prior to 2012, the AADT for Holabird Avenue-.10 MI W of Broening Hwy traffic volume is 12,911 in 2008 and increases to 14,898 in 2011. After 2011, the AADT traffic data increased from 14,772 in 2012 to 17,330 in 2016, while the truck traffic data for this location is 3781. The significant traffic increase from 2008 to 2016 is due to the opening of the Amazon Fulfillment Center in 2012. Figure 2 and Figure 3 show stacked bar charts by vehicle class volume for the years 2010 and 2016.
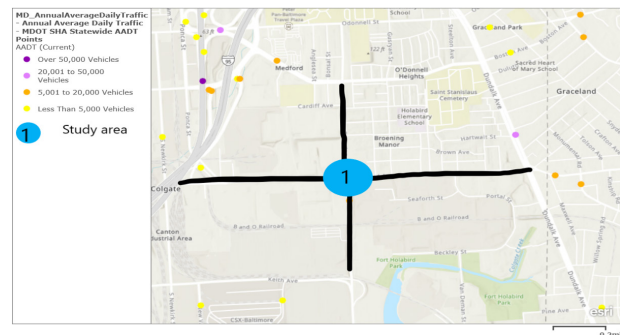
Figure 1. Study Area
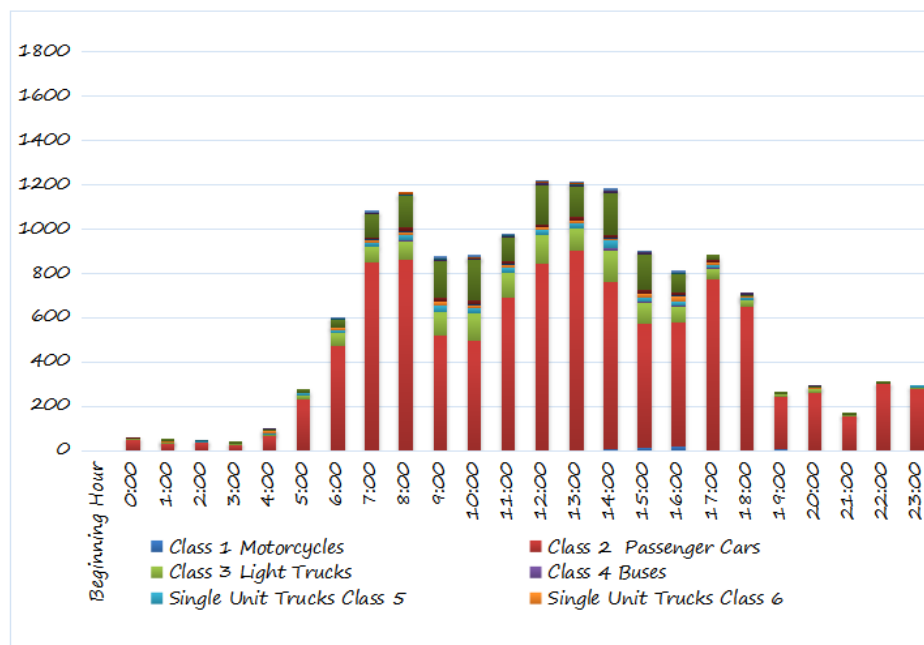
Figure 2. Class Volume Data for 2010
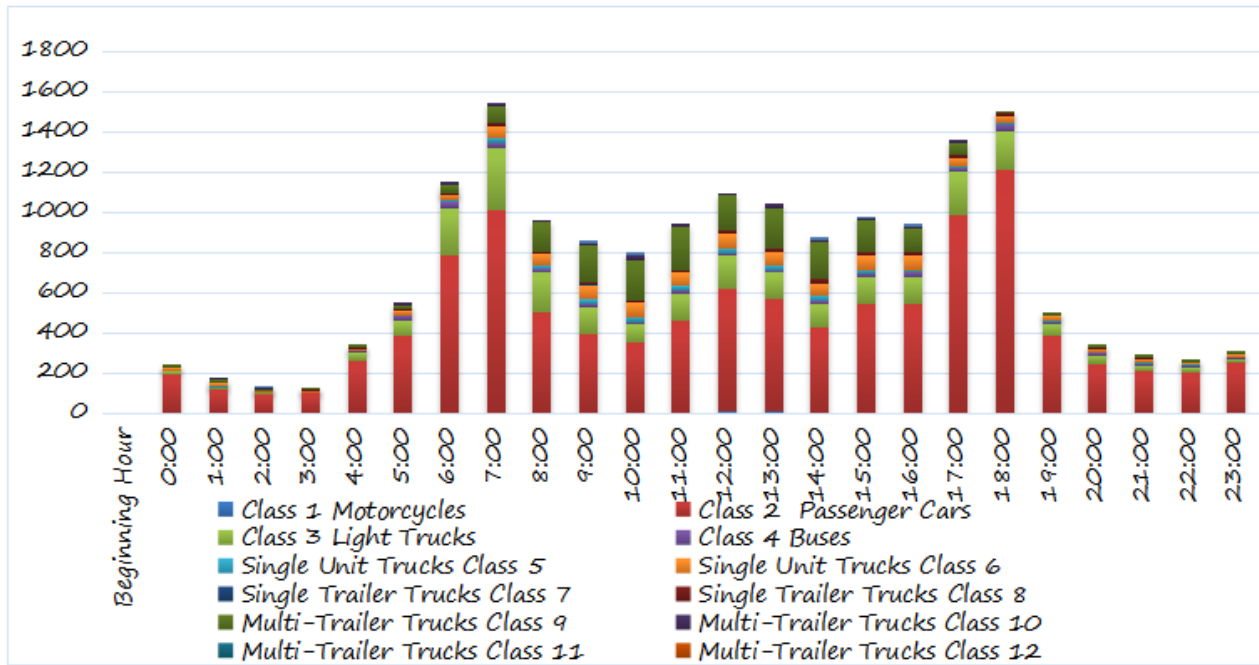
Figure 3. Class Volume Data for 2016

Research Objective

The purpose of this research is to analyze the change in traffic volume and modal splits during the COVID-19 pandemic using existing traffic data and signal timing at an intersection located along a multimodal corridor with a heavy volume of truck traffic. Specifically, the COVID-19 pandemic has caused an increase in e-commerce, thereby increasing the number of freight truck traffic on the road and decreasing passenger car volumes as a lot of employers are demanding their employees telework due to the COVID-19 pandemic. This study will aim at analyzing pre-COVID traffic data and COVID data to see the need to reallocate traffic signal as a result of the sudden change. This research used existing traffic data from bus and freight truck transit agencies such as the MDOT SHA Traffic AADT Monitoring System to analyze freight truck service performance during pre-COVID and COVID.

The research object will take the following form:
- Evaluate the current traffic situation pre-COVID and COVID at the Holabird Avenue and Broening Highway Intersection near the Amazon Fulfillment Center.
- Measure the effectiveness of reallocating traffic signal timing to meet the surge in freight truck volumes under mixed traffic conditions during current COVID-19 and pre-pandemic conditions.

2. Literature Review

Traffic Emissions at Intersection and Air Quality Models

The operational performance at a signalized intersection could be assessed using various traffic performance measures of effectiveness (MOEs) for evaluating the intersection level of service such as average vehicle delays, number of stops, travel time, throughput and traffic capacity, queue length, average fuel consumption, and total vehicle emissions (CO, NOx, HC) [2]. The emissions produced are proportional to fuel consumption, and emissions are usually higher near intersections compared to other street segments [2]. Studies have shown that fuel economy and emissions could be significantly reduced by improving vehicle standards as well as the optimization of traffic management systems [2]. Finally, the author concluded that the optimum MOE estimates along the Pareto front were obtained by optimizing green splits in response to dynamic traffic demand [2]. The proposed algorithm yielded a 22.5% reduction in average fuel consumption and about a 17% decrease in total vehicle emissions.

COVID-19 and Transportation

The demand for movement is directly related to

participation in other economic activities such as work and shopping; the COVID-19 pandemic has demonstrated this fact on a global scale [3]. Transport operations dependent on revenue from reliable travel volumes experienced significant revenue declines, including fare, fuel tax, and toll revenues [3]. Conversely, the demand for transportation and logistics in certain sectors such as e-commerce has surged [3]. Hence, the COVID-19 pandemic has dramatically illustrated the need for transportation professionals to prepare for future disruptions [3].

In Minneapolis, COVID-19 related shut down reduced traffic volume on average throughout the city by 50% [4]. However, the effects proved to be only temporary, after which the traffic volume began to recover at a slow but steady pace [4]. Although passenger vehicle volumes decrease, it is not known how the increase in trucking during the COVID-19 pandemic influenced these traffic counts [4].

In summary, past research has been carried out on signal control strategies pertaining to vehicle delay at a signalized intersection, persons delay on bus transit, and optimization of signal control for multimodal traffic. This study aims to evaluate the pre-COVID and COVID traffic volumes with the existing traffic signal timing and develop a monetized equation based on persons' time, the value of goods for freight trucks, and exhaust emissions. The goal of this research is to look at multiple parameters in one equation at six different scenarios in order to recommend a traffic signal reallocation strategy for an intersection with high volumes of freight trucks before and during the COVID-19 pandemic, thus capturing the shift to teleworking and surge in e-commerce during due to the pandemic.

3. Methodology

Data Collection

As previously mentioned, this study investigates traffic flow at Holabird Ave and Broening Highway in Baltimore, MD. The traffic data were collected on Wednesday, October 2, 2019 (Pre-COVID). The morning peak period 6:00 a.m. to 9:00 a.m., with the peak hour ranging from 7:00 a.m. to 8:00 a.m. The author returned to the site on Wednesday, March 3, 2021 (COVID), to collect traffic data during the COVID pandemic period via video recording from 7:00 a.m. to 8:00 a.m. to align with the SHA peak hour. The existing signal timing for all approaches was also collected in the field on March 3, 2021.

Figure 4 and Figure 5 show the existing lane configuration and phase diagram for Holabird Avenue and Broening Highway. The EB and WB direction has two

through lanes, and EB has an exclusive permissive left-turn lane onto Broening Highway NB. The WB has one exclusive permissive left-turn lane onto Broening Highway SB and a shared right turn lane to Broening Highway NB. Figure 6 is the new recommended 3 phase diagram, the WB has protected left turn into Broening Highway NB and the EB lane has a protected right turn into Broening Highway SB.
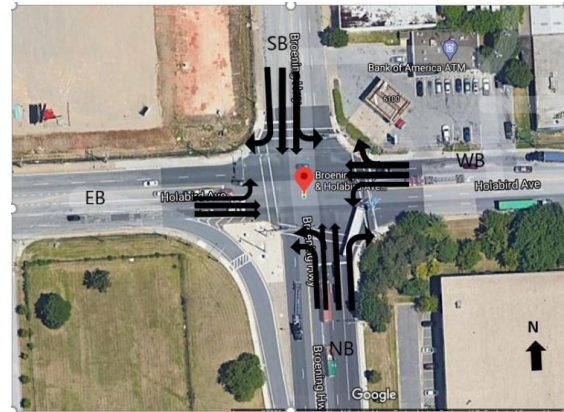
Figure 4. Lane Configuration at Holabird Ave & Broening Hwy

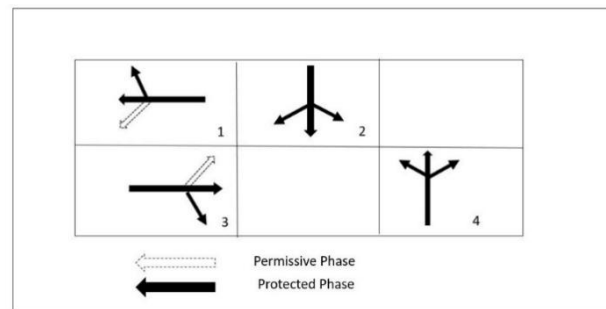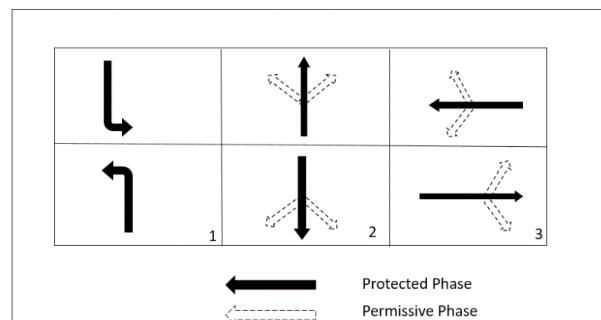**Figure 5.** Exiting 3-Phase Diagram at Holabird Ave & Broening Hwy

Figure 6. New 3-Phase Diagram at Holabird Ave & Broening Hwy

Step 2 will run six scenarios in SYNCHRO to obtain the delay, emissions, and in some scenarios, signal timing. There were three scenarios with pre-COVID volumes and three scenarios with COVID volumes. Additionally, a new 3-phase signal phasing scheme was tested.

The field observed COVID data show that the westbound (WB) approach has the highest traffic volumes for cars during the morning peak (304), while the northbound (NB) approach has the lowest traffic volumes for cars (126). For trucks, the eastbound (EB) and WB approaches have the highest volumes of heavy vehicles (196 and 195, respectively). The NB and southbound (SB) approaches have the lowest volume of heavy vehicles (145 and 129). The number 65 bus runs along this corridor; one bus runs along the EB right (EBR) direction, and two buses in the NB left (NBL) direction. The Peak Hour Factor (PHF) calculated in each direction of approach shows a bit of variability, from 0.80 to 0.93. Traditionally, it is not usually below 0.80 for an urban environment.

Table 1 shows the pre-COVID data on October 2, 2019, from 7:00 a.m. to 8:00 a.m. Similar to the COVID data, the data is classified into cars, buses, and trucks. The overall peak hour factor (PHF) of 0.92 provided by SHA was used in all directions. Since the SHA data was presented by approach and not by movement, the authors assumed that the proportion of vehicles turning left, turning right, and proceeding straight for a particular movement remains the same pre-COVID as it was during COVID for each mode though the total number of vehicles varied.

The pre-COVID data show that the WB approach has the highest total volume of cars (716) while the NB approach has the lowest volume of cars (165). For trucks, the WB, NB, and SB have the highest volumes of heavy vehicles, 72, 78, 100, respectively. The EB approach has the lowest volume of heavy vehicles with a total of 37. The assumption for the number of buses per hour is one on the EBR and two on the NBL. The existing bus schedule also shows that one bus per hour runs on the EBR and two buses per hour NBL direction. The number of buses per hour is two on the NBL movement. While the magnitude of the volumes differed in the pre-COVID and COVID cases, in both the WB approach had the largest volume followed by EB, NB, and SB. Traffic volumes changed between the two data sets.

Table 1 shows traffic volumes by the movement for cars, trucks, and buses. As shown in the traffic volume of cars pre-COVID was higher than during COVID. However, for trucks, the volume of trucks increased during COVID.

While the magnitude of the volumes differed in the pre-COVID and COVID cases, in both the WB approach had the largest volume followed by EB, NB, and SB (see Figure 9 and Figure 10). Traffic volumes changed between the two data sets. Figure 7 and Figure 8 shows traffic

Table 1. Pre-COVID Volumes and COVID Volumes

| Vehicle Type	EBL	EBT	EBR	WBL	WBT	WBR	NBL	NBT	NBR	SBL	SBT	SBR	Total
Pre-COVID Volumes (10/02/2019)													
Cars	43	321	79	146	469	101	69	55	41	94	191	113	1722
		443			716			165			398		
Trucks	4	14	19	32	30	10	37	13	28	28	49	23	287
		37			72			78			100		
Buses	0	0	3	2	4	2	2	0	0	2	3	2	20
		3			8			2			7		
Total	47	335	101	180	503	113	108	68	69	124	243	138	2029
		483			796			245			505		
%HV	9%	4%	22%	19%	7%	11%	36%	19%	41%	24%	21%	18%	
PHF	0.92	0.92	0.92	0.92	0.92	0.92	0.92	0.92	0.92	0.92	0.92	0.92	
COVID Volumes (03/03/2021)													
Vehicle Type	EBL	EBT	EBR	WBL	WBT	WBR	NBL	NBT	NBR	SBL	SBT	SBR	Total
Cars	26	191	47	62	199	43	53	42	31	41	83	49	867
		264			304			126			173		
Trucks	21	74	101	87	80	28	68	25	52	36	63	30	665
		196			195			145			129		
Buses	0	0	1	0	0	0	2	0	0	0	0	0	3
		1			0			2			0		
Total	47	265	149	149	279	71	123	67	83	77	146	79	1535
		461			499			273			302		
% HV	45%	28%	68%	58%	29%	39%	57%	37%	63%	47%	43%	38%	
PHF	0.8	0.88	0.8	0.93	0.8	0.8	0.89	0.8	0.8	0.84	0.87	0.8	
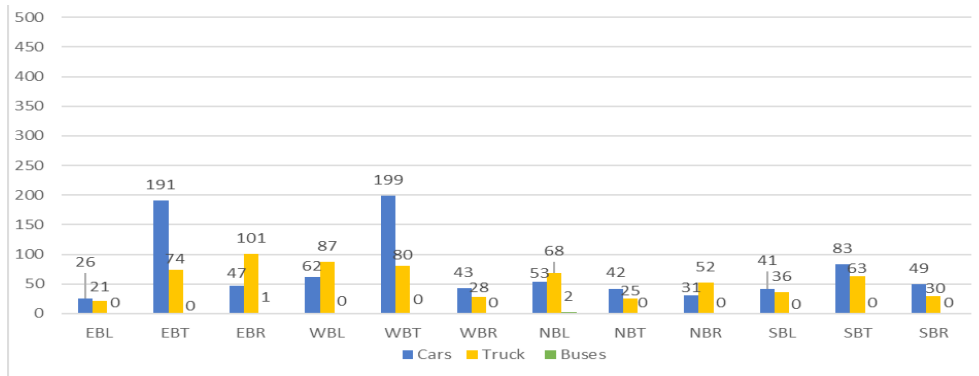
Figure 7. COVID Volumes by Movement
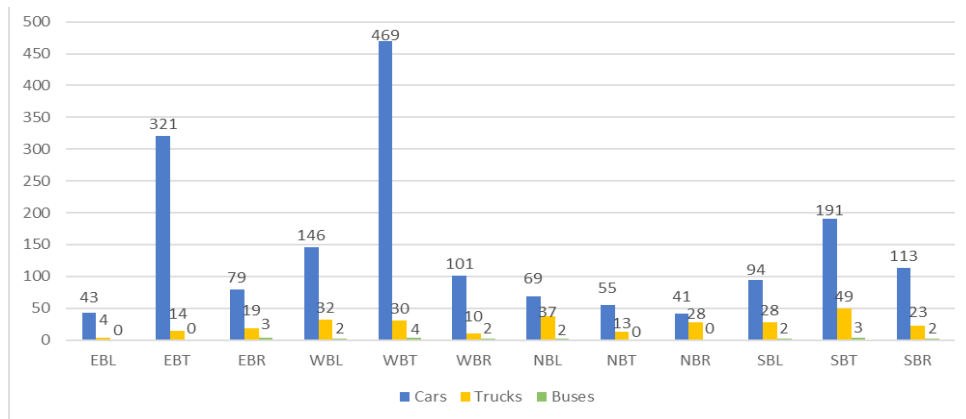

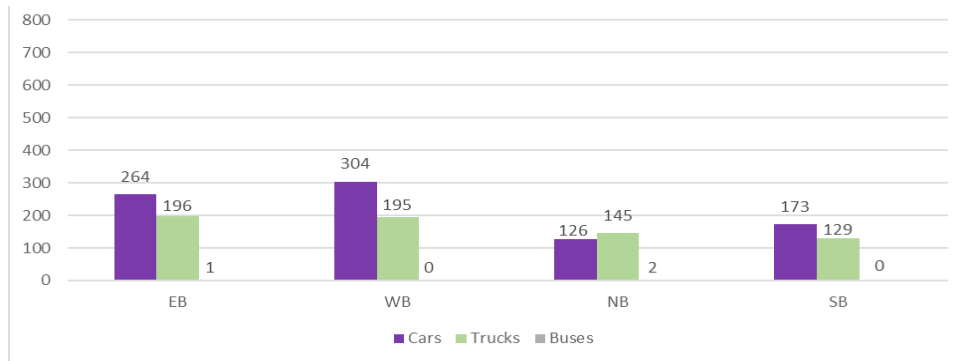**Figure 8.** Pre-COVID Volumes by Movement

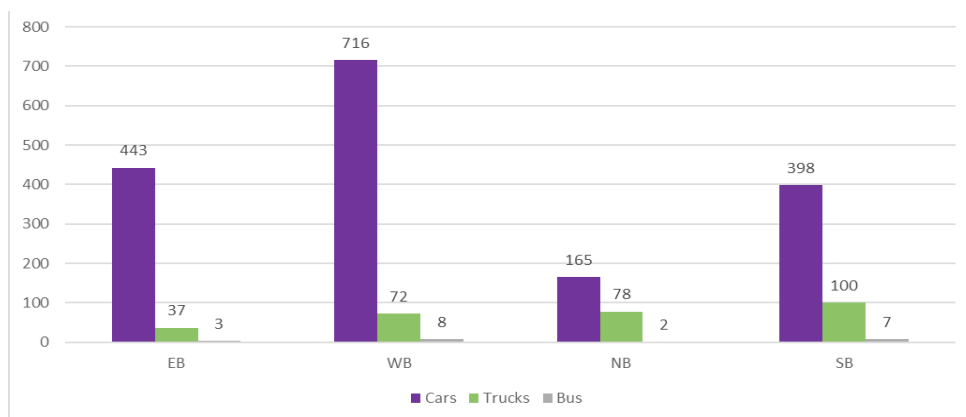

Figure 9. COVID Volumes by Approach

Figure 10. Pre-COVID Volumes by Approach

Table 2. MTA Average Daily Ridership for Route 65 in Fall 2017 and Maximum Load

Service Type	Avg. Number of Riders per Trip	Sampled Round Trip Revenue Hours	Avg. Passenger per Revenue Hour	Sampled Riders	Average Passengers per Mile	Load Factor (% of Seats Filled)
WEEKDAY	20.46	65.2	25.4	744.16	2.260	0.255
SAT	18.93	29.9	23.4	354.20	2.063	0.239
SUN	17.49	36.7	31.7	445.84	1.943	0.226
	Maximum Loads for #65 Stops Serving Holabird Ave and Broening Hwy					
	Maximum Load [pax]		Value of Time [$/hr]			
	East Bound	Northbound	Eastbound	Northbound		
Pre-COVID (Feb 2020)	26	35	$292.61	$382.34		
COVID (Oct 2020)	21	29	$242.76	$322.52		

volumes by the movement for cars, trucks, and buses. As shown in Figure 7, the traffic volume of cars pre-COVID was higher than during COVID. However, for trucks, the volume of trucks increased during COVID.

MTA Bus Ridership Data

Table 2 provides ridership data for Route 65 for Fall 2017. The data counts are from onboard Automatic Passenger Counting (APC) system data; it shows average daily weekday and weekend bus stop ridership (boarding, alighting). The ridership data show bus 65 has a stop located on Holabird Avenue EB by Amazon Fulfilment Center.

A Freedom of Information Act (FOIA) request was conducted to obtain ridership data for the MTA transit system for February 2020 (pre-COVID) and October 2020 (COVID). Since we are analyzing the morning peak period, the maximum load is used for the analysis. The maximum load data was provided at the stop level, while this may slightly overestimate the number of bus riders, the 2017 average weekday ridership numbers shown in Table 2 provide further evidence that the numbers provided in Table 2 are realistic for the weekday morning peak.

Emission Cost

SYNCHRO provides three measures of tailpipe emissions: carbon monoxide (CO), nitrogen oxides (NOx), and volatile oxygen compounds (VOC) in units of grams based on fuel consumption which is a function of speed, vehicle miles traveled, and the number of stops. Given fuel consumption () in gallons, the amount of CO, NOx, and VOC, respectively, is given as:

CO= F x 69.9 g/gal   (1)

NOx= F x 13.6 g/gal   (2)

VOC=F x 16.2 g/gal   (3)

(DelDOT, 2014) [5].

Table 3 illustrates the estimated cost of emissions developed in past studies. The cost estimates in Table 3 were adjusted to 2020 dollars using the United States Bureau of Labor Statistics Inflation Calculator [①]. Additionally, tons were converted to kg use the conversion that 1 ton = 907.185 kg. Thus for this study, we assume that the value of emissions for carbon monoxide, , is $5.85/kg, the value of VOCs, , is $3.36/kg, and the value of NOx, , is averaged to $12.53/kg.

Table 3. Value of Emissions Estimates (Victoria Transport Policy Institute (2011) [6])

Publication	Costs	Cost Value	2020 USD/ ton	2020 USD/ kg
AEA Technology Environment (2005) [7]	NOx	2005 €19,7750	$13,293	$14.65
	VOCs	€1,813	$3,049	$3.36
Wang et al. (1994)	NOx	1989 $/ton $4,430	$9,437	$10.40
	CO	2,490	$5,304	$5.85

Analysis/Result

Table 4 shows the summary of Synchro results for Scenarios 1 to 6. Comparing the cycle length of the Pre-COVID scenarios (Scenarios 1~3), Scenario 1 has the highest at 118 sec compared to 75 sec for Scenarios 2 and 3. For intersection delay, Scenario 1 has the highest delay at 32.0 sec compared to Scenario 2 and Scenario 3, which experienced a delay of 23.2 secs and 18.7 secs, respectively. Scenario 3, pre-COVID volumes with new phasing and optimal signal timing, has the lowest intersection delay (18.7 sec) and operates at a LOS B compared to Scenarios 1 and 2, which have a LOS C. The CO, NOx, and VOC emissions are the highest in Scenario 1. The CO, NOx, and VOC emissions are significantly lower in Scenario 3 compared to Scenarios 1 and 3. In summary, Scenario 3 has the lowest values for all output for the pre-COVID scenarios, as shown in Table 4.

① https://www.bls.gov/data/inflation_calculator.htm

Similarly, Table 4 summarizes Synchro results for the COVID scenarios (Scenarios 4-6). The cycle length in Scenario 1 is the highest at 118 sec, followed by 75 secs for Scenario 5 and 65 secs in Scenario 6. For intersection delay, Scenario 4 has the highest delay, 31.6 secs, compared to Scenarios 5 and 6 at 26.5 sec and 20.3 sec, respectively. While all three COVID scenarios are operating a LOS C, Scenario 6, COVID volumes with new phasing and optimal delay, has the lowest intersection delay. The CO, NOx, and VOC emission is the highest in Scenario 4 and the lowest in Scenario 6. Similar to the Pre-COVID scenarios, the lowest values of all output during COVID occurred in the new phasing and optimal signal timing scenario (Scenario 6) (see Table 4).

Table 4. Summary of Synchro Results

Scenario	Cycle Length (s)	Intersection Delay (s/veh)	LOS	CO (g/hr.)	NOx (g/hr.)	VOC (g/hr.)
1: Pre-COVID, Existing phase & timing	118	32.0	C	2916	567	676
2: Pre-COVID, Existing phase, Optimal timing	75	23.2	C	2663	518	617
3: Pre-COVID, New phasing, Optimal Timing	75	18.7	B	2436	474	564
4: COVID, Existing phase & timing	118	31.6	C	2256	438	523
5: COVID, Existing phase, Optimal timing	70	26.5	C	2155	419	499
6: COVID, New phasing, Optimal timing	65	20.3	C	1948	377	452

4. Discussion of Results

Impact of COVID

The COVID-19 pandemic significantly changed traffic flows across the world. This study looked at an intersection with high freight volume in Baltimore, MD. The Holabird Ave and Broening Highway intersection serves an Amazon Fulfillment Center and the Port of Baltimore. This research collected traffic volumes during COVID (10/12/2019) and compared them with pre-COVID (10/02/2019) traffic volumes. The analysis presented in this research considered six different scenarios measures of performance.

Pre-COVID volumes show a significant change in traffic volumes and further illustrate the impact of COVID on modes of traffic and delay experienced at the intersection. Overall, the percentage change in total

volume was –4.5%, –37.3%, +11.4%, –40.2% along the EB, WB, NB, and SB approaches, respectively. In the study period, car volumes declined by 50%, and truck volumes increased by 130%. This resulted in a high heavy vehicle percentage during COVID. Specifically, the heavy vehicle percentage in EBL, EBT, EBR, WBL, WBT, WBR, NBL, NBT, NBR, SBL, SBT, SBR lanes increased by 36%, 24%, 46%, 39%, 22%, 28%, 21%, 18%, 22%, 23%, +2%, +0%, respectively.

This change in traffic volume and the percentage of heavy vehicles resulted in delay and a need for signal optimization. Using the volume data in Volumes, and signal timing data observed in the field, delay and level of service (LOS) were calculated in Synchro for six scenarios. Comparing the two existing scenarios, Scenario 1: Pre-COVID Existing and Scenario 4: COVID Existing, the LOS remained C, and the overall intersection with delay was 32.0 sec/veh Pre-COVID and 31.6 sec/veh during COVID (see Table 4).

Summary of Contribution

The research contributed to two main areas: (1) increase the understanding of how the COVID-19 pandemic impacted areas with high freight volumes, and (2) provided a methodology for combining multiple performance metrics into a single objective. A methodology was developed to calculate the delay and the cost of carbon monoxide (CO), volatile organic compounds (VOCs), and nitrogen oxide (NOx) emissions.

In Table 4, Scenarios 2 and 5 optimized the signal using the existing phasing. The LOS C remained at C, but the intersection delay dropped to 23.2 sec/veh pre-COVID and 26.5 sec/veh during COVID for Scenario 5 (COVID Optimal). With the new phasing scheme in Scenarios 3 & 6, the intersection delay dropped. Despite the lower total volumes during COVID, the LOS was B Pre-COVID and C during COVID, and the overall intersection delay 18.7 secs and 20.3 secs, respectively.

Traffic volume decreased by 24.3% during COVID at the study location. As a result, the total emissions (in g/hr) for the existing cases (Scenarios 1 & 4) decreased by 22.6%, and comparing the optimized signal timing with new phasing (Scenarios 3 & 6), emissions decreased by 20.0%.

This research provided a baseline understanding of how traffic volumes changed during the COVID-19 pandemic at an intersection that serves two freight activity centers – the Port of Baltimore and an Amazon Fulfilment Center. This study only considers data during the morning peak period due to limitations in manual data collection. Moreover, only one count pre-COVID and one count

during COVID was used; so the results may be subject to natural fluctuations in traffic volume. Future work should consider collecting data over multiple days and multiple time periods using automatic data collection.

The COVID analysis showed that the shift to teleworking and reliance on e-commerce impacted the volume and modal split of traffic and demonstrated the need for signal adaption during disruptive events. The findings of this study could provide useful guidance to traffic engineering professionals and policymakers to prepare for a future crisis that can disrupt the traffic system. Future research could focus on more efficient computational algorithm techniques to solve traffic signal optimization during disruptive events or pandemic.

Author Contributions

All authors contributed to all sections of this report and have reviewed the results and approved the final version of the manuscript.

Conflict of Interest

There is no conflict of interest.

References

[1] Hendrickson, C., Rilett, L.R., 2020. The COVID-19 pandemic and transportation engineering. American Society of Civil Engineers. https://ascelibrary.org/doi/full/10.1061/JTEPBS.0000418.AEA Technology Environment. (2005). Damages per tonne emission of PM2.5, NH$_3$, SO$_2$, NOx and VOCs from each EU25 Member State (excluding Cyprus) and surrounding seas.

[2] Al-Turki, M., Jamal, A., Al-Ahmadi, H.M., et al., 2020. On the potential impacts of smart traffic control for delay, fuel energy consumption, and emissions: An NSGA-II-based optimization case study from Dhahran, Saudi Arabia. Sustainability. 12(18), 7394.
DOI: https://doi.org/10.3390/su12187394

[3] Hendrickson, C., Rilett, L.R., 2020. The COVID-19 pandemic and transportation engineering. American Society of Civil Engineers. https://ascelibrary.org/doi/full/10.1061/JTEPBS.0000418. AEA Technology Environment. (2005). Damages per tonne emission of PM2.5, NH$_3$, SO$_2$, NOx and VOCs from each EU25 Member State (excluding Cyprus) and surrounding seas.

[4] Liu, Z., Stern, R., 2021. Quantifying the traffic impacts of the COVID-19 shutdown. Journal of Transportation Engineering, Part A: Systems. 147(5), 04021014. https://ascelibrary.org/doi/10.1061/JTEPBS.0000527.

[5] DelDot, 2014. Estimating Vehicle Emissions in Signalized Networks with Synchro/SimTraffic.

[6] Victoria Transport Policy Institute, 2011. Transportation cost and benefit analysis II – air pollution costs. Victoria Transport Policy Institute.

[7] AEA Technology Environment, 2005. Damages per tonne emission of PM2.5, NH$_3$, SO$_2$, NOx and VOCs from each EU25 Member State (excluding Cyprus) and surrounding seas.

EDITORIAL

Glazing Systems for Reaching Net Zero Energy Buildings Target

Müslüm Arıcı[*]

Mechanical Engineering Department, Engineering Faculty, Kocaeli University, Umuttepe Campus, Kocaeli, 41001, Turkey

The increasing trend of global energy demand due to rising population, comfort expectations and living standards has caused a prevalent concern about the state of the supply-demand chain of energy in the upcoming years. Considering that the building sector is responsible for about one-third of the final energy demand and related greenhouse gas emissions, it is important to take actions in order to reduce the energy demand of building sector and consequent release of greenhouse gas emissions [1]. Moreover, energy need of the globe is expected to be doubled by 2050. In this context, the concept called Net Zero Energy Buildings (NZEBs) stands as a promising solution to the problem since it offers energy-efficient and high-performance buildings, and healthy indoor environments. Furthermore, NZEB can significantly cut down the indirect greenhouse gas emissions due to the reduction in energy demand.

Utilization of renewable energy systems, such as solar energy, as well as reducing energy consumption of the buildings through improving thermal resistance of the building envelope is an essential need for NZEBs. The overall heat transfer coefficient (U-value) of both opaque and transparent building envelope has a significant role in the cooling and heating consumption of buildings. The U-value of opaque building envelopes such as external wall, roof, and floor of buildings can be easily reduced by installing insulation materials. On the other hand, this is more challenging for the glazing units which are essential construction components of the buildings, providing natural lighting, visibility, and spacious feeling. The thermal performance of conventional glazing systems is low due to their low thermal resistance, in comparison with other opaque envelope elements. Moreover, thermal mass of glazing systems is much lower than these building components. Since glazing units can account up to about 30-50% of heat loss from a building [2], a significant

Corresponding Author:
Müslüm Arıcı,
Mechanical Engineering Department, Engineering Faculty, Kocaeli University, Umuttepe Campus, Kocaeli, 41001, Turkey;
Email: muslumarici@gmail.com

amount of research has been focused on improving their thermal performance. Regarding this focus point, the most common technique to reduce heat transmission through windows is to use double glazing systems instead of single glazing ones, which can easily decrease heat transfer more than 50%. Optimizing the air layer between panes to hinder air movement thus maximizes the thermal resistance. With this aim, replacing the air by noble gasses (such as argon, krypton) whose thermal conductivity is lower than that of the air, increasing number of panes (i.e., triple and even quadruple panes), and coating the glazing surfaces to control solar heat gain are among the most used techniques.

Filling the gap between multiple pane windows with aerogel or phase change material (PCM) is relatively a novel technique. Although the discovery of aerogel dates back to 1930s for space applications, the interest in usage of these materials in buildings has been emerging since 1980s [3]. Aerogels have significantly low thermal conductivities and high transparency, making them attractive materials for glazing systems. PCMs can absorb or release a significant amount of thermal energy during the melting or solidification process due to the latent heat of fusion. The temperature of PCM remains nearly the same during the phase change process. This feature makes them a promising option for glazing units. Thus, incorporating PCM in the glazing systems helps improving effective utilization of solar energy through absorbing solar energy (melting process) during the daylight hours and releasing it during the nocturnal hours (solidification process). Moreover, apart from reducing energy consumption and improving thermal comfort in the indoor environment, it helps shifting the cooling and heating energy consumption of buildings to off-peak periods, increases thermal mass of the glazing unit, and providing flexibility for energy usage in buildings. The phase transition temperature should be selected properly considering the climatic conditions in order to effectively exploit the latent heat of PCM. Optical properties of PCM should also be considered for applications particularly where the visual transmittance of PCM is important since the visual transmittance of the solid state of the PCM (such as paraffin) decreases from 90% to 40% in the liquid state [4]. Optical properties are significant for smart glazing systems where the light and solar energy transmission can be changed. Apart from the aforementioned purposes, windows can be used for harvesting solar energy also through integrating photovoltaics into windows.

To sum up, although a considerable enhancement in the thermal performance of glazing units has been achieved through the above-mentioned methods, there is still a considerable room for further improvement. Therefore, more effort is needed within the context of the net positive-, net zero-, or nearly zero energy buildings.

Conflict of Interest

There is no conflict of interest.

References

[1] Energy Efficiency 2018—Analysis and Outlooks to 2040, International Energy Agency Publications, France, 2018.

[2] Arıcı, M., Tükel, M., Yıldız, Ç., et al., 2020. Is the thermal transmittance of air-filled inclined multi-glazing windows similar to that of vertical ones?. Energy and Buildings. 229, 110515.

[3] Buratti, C., Belloni, E., Merli, F., et al., 2021. Aerogel glazing systems for building applications: A review. Energy and Buildings. 231, 110587.

[4] Gowreesunker, B.L., Stankovic, S.B., Tassou, S.A., et al., 2013. Experimental and numerical investigations of the optical and thermal aspects of a PCM-glazed unit. Energy and Buildings. 61, 239-249.